Truthful visualizations for mass spectrometry imaging enable high spatial resolution interactive m/z mapping and exploration

Jacob Gildenblat[1] and Jens Pahnke[1,2,3,4,5,6*]

[1*]Pahnke Lab, www.pahnkelab.eu.
[2*]Translational Neurodegeneration Research and Neuropathology Lab, Department of Clinical Medicine, Medical Faculty, University of Oslo, Sognsvannsveien 20, Oslo, NO-0372, Norway.
[3*]Section of Neuropathology Research, Department of Pathology, Division of Laboratory Medicine, Oslo University Hospital, Sognsvannsveien 20, Oslo, NO-0372, Norway.
[4]Institute of Nutritional Medicine, University of Lübeck and University Medical Center Schleswig-Holstein, Ratzeburger Allee 160, Lübeck, D-23538, Germany.
[5]Department of Neuromedicine and Neuroscience, The Faculty of Medicine and Life Sciences, University of Latvia, Jelgavas iela 3, Riga, LV-1004, Latvia.
[6]Department of Neurobiology, School of Neurobiology, Biochemistry and Biophysics, The Georg S. Wise Faculty of Life Sciences, University of Tel Aviv , G. S. Wise Street, Ramat Aviv, IL-6997801, Israel.

*Corresponding author(s). E-mail(s): jens.pahnke@gmail.com;
Contributing authors: jacob.gildenblat@gmail.com;

Abstract

Mass Spectrometry Imaging (MSI) provides complex molecular profiling pivotal for advanced biochemical analysis and diagnostics. We have identified an urgent need for computationally sophisticated, interactive, and automated visualization tools specifically designed for MSI analysis that employ dimensionality reduction (DR) methods to preserve global data structure. We present MSI-VISUAL, an open-source framework that enables rapid and intuitive MSI data exploration, providing panels of truthful visualizations and virtual pathology stains (VPS),

with automatic and manual region selection, real-time verification, and statistical comparisons. Integrating established DR techniques, MSI-VISUAL introduces four novel visualization strategies: Saliency (SALO) and Spearman (SPEAR) Optimizations enhance global structure preservation across various distance metrics, addressing significant visualization challenges; TOP3 and Percentile Ratio (PR3D) provide memory-efficient and computationally rapid visualizations for large-scale datasets. In this work, comprehensive benchmarking and biological examples confirm that our DR visualizations surpass existing methods, facilitating the determination and quantification of subtle tissue differences at a single-cell level, revealing novel biological insights, and enabling diagnostic applications.

Keywords

mass spectrometry imaging, medical imaging visualization, virtual pathology stain, dimensionality reduction, segmentation, saliency optimization, global structure preservation, percentile ratio, clustering, PCA, NMF, K-means, PaCMAP, UMAP, t-SNE, SALO, SPEAR, PR3D, TOP3, ALS, Alzheimer's disease, β-amyloid, brain, kidney, spinal cord, α motor neuron, pathology

Abbreviations

Aβ – amyloid-β
AD – Alzheimer's disease
ALS – amyotrophic lateral sclerosis
DR – dimensionality reduction
IHC – immunohistochemistry
MSI – imaging mass spectrometry
NMF3D – 3-dimensional, non-negative matrix dimensionality reduction
PaCMAP – Pairwise Controlled Manifold Approximation
PCA – principal component analysis
PR3D – 3-dimensional percentile ratio dimensionality reduction
ROI – region of interest
SALO – saliency optimization dimensionality reduction
SPEAR – Spearman correlation optimization for dimensionality reduction
TIC – total ion current
TOP3 – top 3 m/z values dimensionality reduction
TriMap – triplet constraints mapping
t-SNE – t-distributed stochastic neighbor embedding
UMAP – uniform manifold approximation
VPS – virtual pathology stain

Introduction

Mass spectrometry imaging (MSI) is a powerful analytical tool that generates intricate datasets, enabling the visualization of biological and functional architectures through the profiling of metabolites, lipids, and proteins for research and clinical applications. MSI offers critical insights that are often inaccessible via conventional histopathological techniques or other imaging modalities [1–5]. MS images are typically represented as high-dimensional images of shape Rows x Columns x N, where N is the number of molecular measurements per point (also referred to as MS spectra). Each pixel in the image has an associated mass/charge (m/z) spectrum with N values. If an m/z measurement does not align perfectly with a predefined bin, its intensity is typically summed into the closest bin. Mapping from N to 1 or 3 dimensions is needed to visualize these high-dimensional images for humans. The experimental or diagnostic use of MSI can only be achieved if the data are visually presented in a way that allows key features and rare events to be easily detectable and confirmable, comparable to a panel of different, but specific histology stains.

To access and exchange MSI data, Schramm et al. [6] introduced imzml, an open-source format for MSI. This is very useful for decoupling the computational methods for MSI visualization and analysis from the generating hardware. Several open-access MSI tools and data repositories with analytical capabilities are available (non-exhaustive list): Cardinal [7], MSIToolbox [8], and the METASPACE repository [9] harboring numerous, freely available MSI datasets.

Regarding the application for experimental or diagnostic use, we identified vulnerable limitations of the data visualizations with the current approaches that we focus on in this study. We found only limited support for advanced, modern MSI visualization methods. Previous work for presenting high-dimensional MSI data mainly relies on different clustering and segmentation methods, such as K-means [10, 11] or on dimensionality reduction (DR) methods, such as UMAP [12**?** –14], which is not widely used in the MSI field despite its prominence in spatial transcriptomic analyses.

In clustering methods, which are most commonly used for visualization of MSI and are well integrated into MSI tools, each image pixel is assigned to a cluster and is colored by the assigned cluster color (reviewed in [15]). This leads to hard borders between categories.

In DR methods, individual features of the transformed data with reduced dimensions can be visualized as images, resulting in multiple summary images of the data or a large panel of visualizations. If the reduction is performed in three dimensions (3D), the dimensions can be interpreted as Red/Green/Blue (RGB) channels and visualized as a color image.

An important point to emphasize is that clustering methods assign the same label to all pixels within a cluster, making them unable to distinguish subtle differences within those groups. In contrast, DR methods assign continuous RGB values to each pixel, allowing the visualization of fine-grained variations, even between spectrally similar regions.

In practice, we find that clustering approaches often fail to reveal visual detail within clusters, leading to a loss of anatomical information that is essential for experimentalists and diagnostics. K-means clustering is sensitive to binning and frequently misses fine details that are incorrectly grouped with broader anatomical regions (Supplementary Information, Figures 13, 14, and 17).

Furthermore, clustering-based visualizations do not preserve any meaningful relationships between cluster colors. This means that anatomically or molecularly similar regions may be assigned arbitrarily different colors, obscuring their biological relevance and disabling the visual quantitative assessment. Visual quantitative assessment is routinely used in pathology diagnostics, applying different histology stains and assessing the intensities and distribution of different colors.

While clustering remains a practical, fast, and widely adopted tool in MSI analysis, MSI-VISUAL advocates for the broader adoption of DR-based visualization methods, which we demonstrate can preserve and reveal greater spatial and molecular detail. Such detail —e.g., identifying single cells or clonal structures in a cancer sample— may be critical for diagnostic and experimental research applications.

UMAP [16], a modern and widely used DR method, has been introduced for MSI in [17], highlighting the effects of different distance metrics on the resulting visualization. Additionally, the use of a Self-Organized Map [18] has been proposed in [19], along with the introduction of the Distance Correlation Metric (DCM) for evaluating MSI visualizations. The DCM is an application of a global structure preservation metric for DR. Global structure preservation is concerned with maintaining relationships between groups of points in the high-dimensional data and the transformed low-dimensional data. For example, if we have three points, where two are close to each other and the third is far from both, the global structure is preserved if the relationship is retained in the low-dimensional space. In other words, a biologist or a pathologist can determine subtle tissue differences in such visualizations.

For MSI and its diagnostic or experimental applications in medicine or biology, global structure preservation is especially essential. Consider the case of small anatomical structures such as metabolite deposition in storage diseases, pathological protein accumulations, e.g., β-amyloid (Aβ) plaques in Alzheimer's disease (AD), single cells, such as motor neurons of the spinal cord, or infiltrating, metastasizing cancer cells. These structures have a distinct m/z content compared to the surrounding region, but also share many m/z features. For example, Aβ plaques would accumulate m/z values from their surrounding brain structures. To ensure that such small and distinct structures become visible in MSI visualizations and usable for experimental setups or diagnostics, we need to preserve the global structure of the high-dimensional data. Meaning, to maintain the visual contrast in visualizations between the target structures and the surroundings, even when shared m/z content exists. Detail-rich anatomical regions, such as the brain stem, present another challenge. Many m/z features are shared across different sub-regions and nuclei, which can bias visualization methods to assign them the same color, as is done in clustering methods.

In extreme but common cases, sub-regions become indistinguishable for the viewer, thus experimentalists lack important information, e.g., of metabolite distribution changes in experiments, or pathologists miss important diagnostic features. This lack

of differentiation also makes it problematic for MSI users to annotate and explore sub-regions (ROI) in their tissue samples, e.g., for the evaluation of treatment effects of subclones in a cancer sample. Strong global structure preservation is essential for revealing these internal tissue variations and ensuring that sub-regions do not appear overly homogeneous. Currently, ROI mapping is used to co-register histology stains and MSI data [5]. However, appropriate truthful visualizations of MSI would allow for generating panels of visualizations without the need of supplementing tissue stains.

The choice of distance metrics is another critical factor [17, 19]. Some structures are defined anatomically —e.g., differences between brain cortex layers— or functional differences —e.g., nuclei of the thalamus, manifest through numerous small changes in m/z values. Others are defined by changes in only a few specific m/z values, as seen with Aβ plaques or cancer subclones. Different distance metrics may be needed to effectively highlight specific structures.

Many DR methods could be applied to MSI data [20]. Classical methods include PCA [21], FastICA [22], Isomap [23], and NMF [24]. Modern methods include UMAP [16], t-SNE [25], and techniques designed to enhance global structure preservation, such as Trimap [26], PaCMAP [27], and Phate [28].

PCA [21] is a gold-standard method for global structure preservation. It finds a linear projection that maximizes data variance. Distances between points on the principal component hyperplanes are fully preserved, ensuring global structure retention. However, when reducing MSI data to just three components from thousands of m/z features, PCA may distort the global structure for points far from the principal components. PaCMAP [27] is a recent method that aims to improve global structure preservation in UMAP. Like UMAP, it creates a graph structure with edges between different points, but it expands the edges to include pairs of points that are far apart. This approach indirectly enhances global structure preservation.

Despite these advancements, no previous work has been done to specifically design MSI-optimized visualization methods. Such methods would need to address MSI-specific challenges, including the robustness of different distance metrics, the extremely high dimensionality of MSI (often with thousands of features per pixel), and the necessity for sufficient computational resources. Additionally, especially for diagnostic use, visualizations must be evaluated based on their effectiveness in revealing specific or even hidden details within MS images.

From a pathologist's standpoint, MSI provides extremely rich datasets that can be used to answer a wide range of basic and applied questions. The prevailing challenge lies in rendering intuitive data presentations through reliable, truthful visualizations that preserve data structures yet facilitate feature detection.

In this work, we present MSI-VISUAL, an open-source framework for extracting, visualizing, and directly interacting with MSI data, robust visualization methods for high global structure preservation in MSI, lightweight visualization methods for large MSI datasets, a benchmarking of these methods, a data presentation named SpecQR, and several analytical examples of experimental and diagnostic use.

Results

Rapid exploration and mapping of MSI data

The MSI-VISUAL framework supports MSI analysis by providing an easy-to-use graphical user interface (GUI) for data extraction, generating multiple user-guided visualizations, selecting and comparing regions of interest (ROI), and mapping significant m/z values, reducing the time and effort required for MSI interpretation (Figure 1).

First, users create a data pipeline to extract the raw MSI data (either in the open source imzml-format [6] or with additional current support for the Bruker hardware format) to a fixed shape tensor of width $rows \cdot cols \cdot N$ in the open source .npy format. N, the number of features per pixel, is determined by the total range of m/z values in the scan and the number of bins allocated for each m/z unit of 1 Da.

Multiple, tunable visualizations can be created of the high-dimensional tensor to provide a multi-visualization panel, where different visualizations may be better for revealing anatomical or functional details of interest in different parts of the image. Then, users can interact with these visualizations by selecting ROIs. MSI-VISUAL supports several modes for ROI selection that allow rapid interaction with the raw MSI data through the visualizations:

1. Manual annotation of regions: In this mode, the user annotates polygons around ROIs in different visualizations of the same MSI scan.
2. Automatic segmentation and clicking on selected regions: In this mode, first, the visualizations are spatially segmented. We use the classic Felzenszwalb-Huttenlocher spatial segmentation method [29] and convert the MSI visualization to sub-regions. These regions are then selected by clicking.
3. Point selection: In that mode, users click on points to focus on smaller structures.

Once ROIs are selected, MSI-VISUAL compares their m/z content and searches for m/z values that are sufficiently different between the ROIs. These m/z values are then displayed as a table and a SpecQR, a graphical visualization that aggregates the m/z spatial images and displays noticeable m/z values on a 2D grid ('QR code')(Supplementary Information, Figure 15). The intensity of the squares in the SpecQR is modulated by the statistical score of the detection m/z values. The aggregation serves as a visual verification for the comparison of the ROIs - if the two regions are separable, there will be a strong visual difference highlighted through red and green color pixels representing specific m/z values. The user may then click on individual m/z values in the table to obtain a Virtual Pathology Stain (VPS) of single m/z images (often termed ion images), for visual verification that these m/z values correspond to the tissue pattern that is searched for.

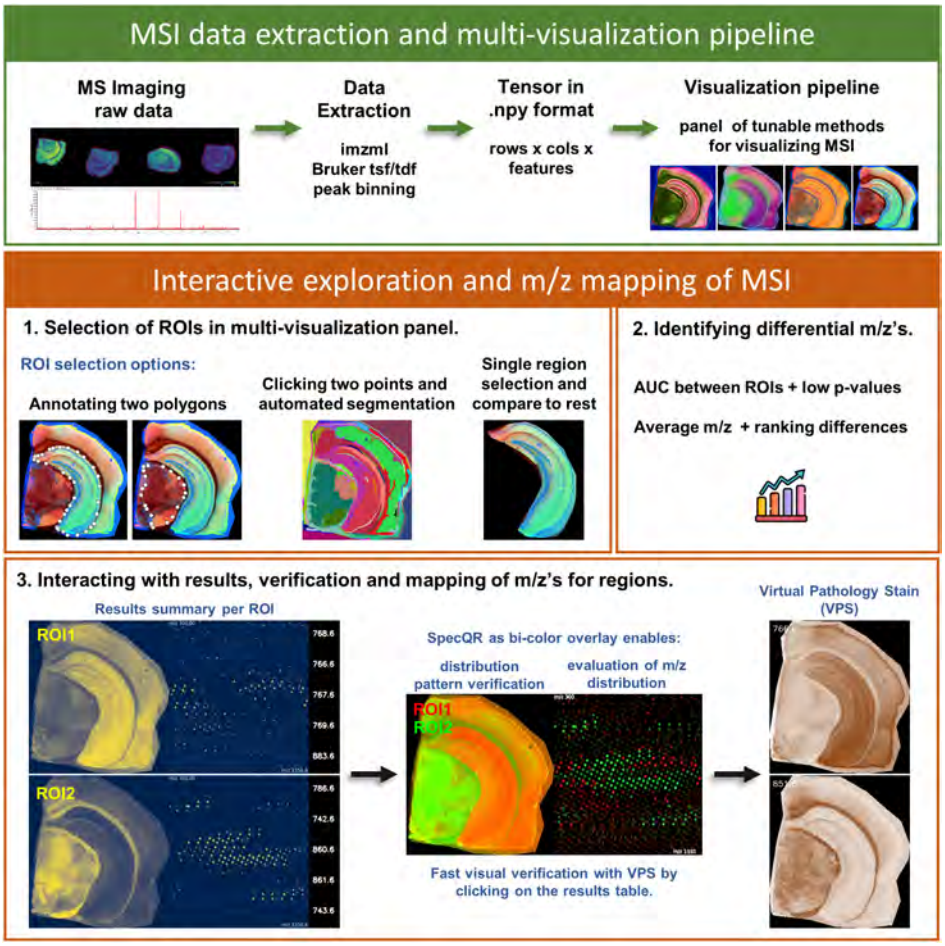

Fig. 1 The MSI-VISUAL workflow consists of different stages: MSI data extraction and a visualization pipeline, interactive exploration with visualization, ROI selection, m/z mapping, and results table, and confirmatory representations as mono (Cividis color scheme [30]) or bi-color images (red-green) or SpectrumQR 2D graph (SpecQR) and Virtual Pathology Stains (VPS, mimicking immunohistochemical (IHC) stains), enabling fast visual evaluation of the ROI properties.

Robust visualization methods for high global structure preservation

We propose Saliency Optimization (SALO) and Spearman Correlation Optimization (SPEAR) to address the next two MSI visualization requirements:

i) High global structure preservation for revealing anatomical details in sub-regions. This is achieved by direct optimization of the global structure preservation. These methods sample a group of representative reference points in the image and optimize an objective on the ranks of the distances of all image pixels from the reference points in the high-dimensional data and the visualization. Both SPEAR

and SALO rely on a differentiable approximation of the ranking operation [31]. The SPEAR visualization optimizes the Spearman rank correlation [32]. The SALO visualization optimizes a new objective we term *Saliency*, which requires ranks of point pair distances in the visualization (in the LAB color space to improve perceptual differences) to be at least as high as in the MSI data, ensuring detail is preserved. Compared to PCA, our methods are non-linear and non-parametric and are able to model complex relationships in the data compared to a linear projection. Compared to UMAP [16], which focuses on local point neighborhoods and local structure preservation, our methods focus specifically on global structure preservation. The idea in PaCMAP [**?**] of sampling pairs of points that are far from each other is somewhat related to our sampling of reference points. However, unlike PaCMAP, we directly target global structure by maximizing the distance correlations, therefore optimizing the global structure preservation, considering relationships between multiple points at once. This achieves higher global structure preservation on the mouse brain dataset (Supplementary Information, Figure 19), SALO receives an average correlation of approximately 0.8, and PaCMAP approximately 0.45.

Furthermore, since we avoid the graph structures of UMAP and PaCMAP, our methods are simpler to implement, have a lower memory footprint, and therefore, are more scalable. On some larger MS images, we were not able to run UMAP even on very strong hardware (Supplementary Information, Figure 21).

ii) Robustness to different distance metrics. The Euclidean (and similarly the Cosine) distances are sensitive to changes in many m/z values at once. The L_∞ distance targets large changes in a single m/z. SALO and SPEAR achieve robustness to both by fusing the Euclidean and L_∞ norms by taking the maximum of their ranks.

Lightweight visualization methods for large MSI datasets

Next, our goal was to design visualizations that are extremely fast to compute and can handle large datasets that other methods fail on because of the extensive computational requirements, even if binning with 5 bins (0.2 Da resolution) is applied. Furthermore, there is a common need for creating thumbnails or quick initial visualizations in MSI viewers. Often, this is done with the total ion current (TIC), followed by colorizing the image, e.g., with the Cividis color scheme [30]. While TIC is a useful lightweight visualization in one dimension, it has only a limited ability to distinguish between image regions as needed for diagnostic assessments. We consider the problems of visualization in a colorful image.

The motivation for these lightweight visualizations is the observation that, in our mouse brain dataset, most image pixels have a small number of dominating m/z values with high intensities (with roughly 75% having one dominating m/z, 20% having two m/z values, and the remaining three or more). The proposed TOP3 visualization simply measures the three largest intensities in each pixel (and then, after outlier removal, converts these from the LAB color space into RGB). The proposed Percentile-Ratio (PR3D) visualization is a generalization of this and measures ratios of fixed, pre-determined percentiles of the intensities. As shown in Supplementary Information, Figure 21, both of these methods are computationally lightweight, with low memory

footprints, and they are hundreds of times faster to compute. This enables faster computation of MSI visualizations for scans with larger computational requirements (either more pixels, more m/z values, or less binning) that other methods fail to address.

Performance evaluation of the MSI visualizations

To quantitatively evaluate the performance of our proposed MSI visualizations, we benchmarked them on two datasets (Methods section, Supplementary Information Tables 1, 2) representing different scenarios, using well-established metrics that have been previously used for MSI [19, 33**?**]. We benchmarked against modern methods: UMAP [16], PaCMAP [**?**], Phate [28], t-SNE [25], TriMap [26] as well as classic methods: PCA [21], NMF [24], Isomap [23] and FastICA [22]. The averaged results across images are presented in Supplementary Information, Figure 19. The proposed SALO visualization performs better than the previously existing methods on all datasets, and also for all individual images in competition with the proposed SPEAR (i.e., not only on average)(Supplementary Information, Figure 20). Our proposed methods, SALO and SPEAR, outperform all existing approaches on both datasets. Additionally, TOP3 achieves the best performance among existing methods for the L_∞ distance. TOP3 and PR3D show competitive performance, with TOP3 consistently outperforming UMAP while maintaining much lower memory requirements and significantly faster computation on larger images (Supplementary Information, Figure 21). However, PR3D struggles with the diverse dataset, highlighting the need for future work on efficient hyperparameter auto-tuning of the percentiles used in PR3D.

Visualization scalability for processing large images

We evaluated the scalability of our methods for large MSI datasets by testing them on a 5µm-resolution, human kidney needle biopsy (Supplementary Information, Table 2, dataset 4). The size of this image is 550×824 pixels with 5,255 features, resulting in a 9.3GB .npy file. We assessed memory usage and runtime, as shown in Supplementary Information, Figure 21. Despite using high-performance hardware with 320GB RAM, several methods —including UMAP— fail to complete due to excessive memory requirements. TOP3 demonstrates exceptional efficiency, running over 600× faster than PaCMAP while consuming only 2MB of additional memory, compared to approximately 17.5GB required by PaCMAP and SALO (approximately twice the image size). SALO measures two types of distances from each image pixel to the reference points ($N = 1,000$ by default), resulting in a memory consumption of Rows x Cols x 1000 * 2 floating point values. A lower number of reference points could be traded off to fit memory. These results highlight the practical advantages of TOP3. While it achieves competitive global structure preservation, it does not match the performance of SALO. However, its high speed and minimal memory footprint make it particularly well-suited for fast visual exploration of large MSI datasets.

The proposed visualizations better reveal histomorphological details

To be able to assess the practical improvements of the new visualizations for the experimentalists or pathologists, we needed to analyze examples that include small, known histomorphological details.

i) Detecting circumscribed small pathological detail:

Aβ plaques are easily detectable with a H&E stain in our mouse model (Supplementary Information, Figure 28) and appear in different sizes and at different locations [34, 35]. These are circumscribed, highly pathological structures also accumulating lipids [36–38]. They change their peptide and lipid composition over time [39, 40]. Figure 2 demonstrates the improved detection of the histopathological changes using the new visualizations. The data used to assess the detection is a lipidomics MSI scan of a mouse brain hemisphere (bregma –2.06 mm, pixel resolution of 20 μm) of a 100-day-old Alzheimer's disease mouse with numerous small and large Aβ plaques. Whereas UMAP detects only very extensive lipid accumulations in the center of large Aβ plaques (dense cores), the proposed visualizations SALO, SPEAR, TOP3, and PR3D highlight numerous contrasted, importantly also small Aβ deposits. K-means segmentation misses these plaques totally and does not assign a specific category (Supplementary Information, Figure 14).

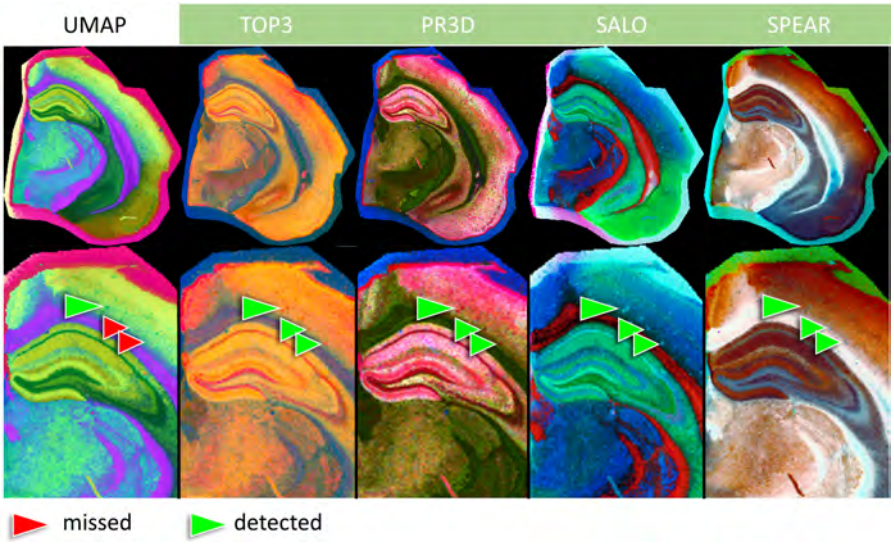

Fig. 2 Improved detection of small pathological details in the brain of an Alzheimer's disease mouse model. The detection of small histopathological, disease-related objects is of importance for treatment development and can be better facilitated using the proposed visualizations (TOP3, PR3D, SALO, and SPEAR). Most Aβ plaques are missed using UMAP (marked with red arrows), and only the center of large plaques is highlighted. Anti-amyloid treatment desolves plaques from their surface; here, detecting small plaques in the different anatomical regions, e.g., hippocampus and cortex, is of specific importance for the effect evaluation.

Parenchymal organs, such as the kidney, have a defined histomorphological appearance with several substructures and sub-regions. The kidney consists of many functional units, each comprising a glomerulus in the cortex and a connected tubulus system reaching from the cortex to the medulla. Figure 3 shows two visualizations highlighting these anatomical details in a glomerulonephritis disease case using MSI with a pixel resolution of 5 μm (see also Supplementary Information, Figure 24). SALO clearly shows the different parts of the tubulus system (proximal and distal tubuli, collection tube) as well as the numerous inflammatory cells between the tubuli and around the glomeruli in their typical pattern. The number of glomeruli is reduced, and the few remaining are strongly pathologically changed. SALO also enables clear detection of remaining glomerulus capillaries and single inflammatory cells, e.g., lymphocytes.

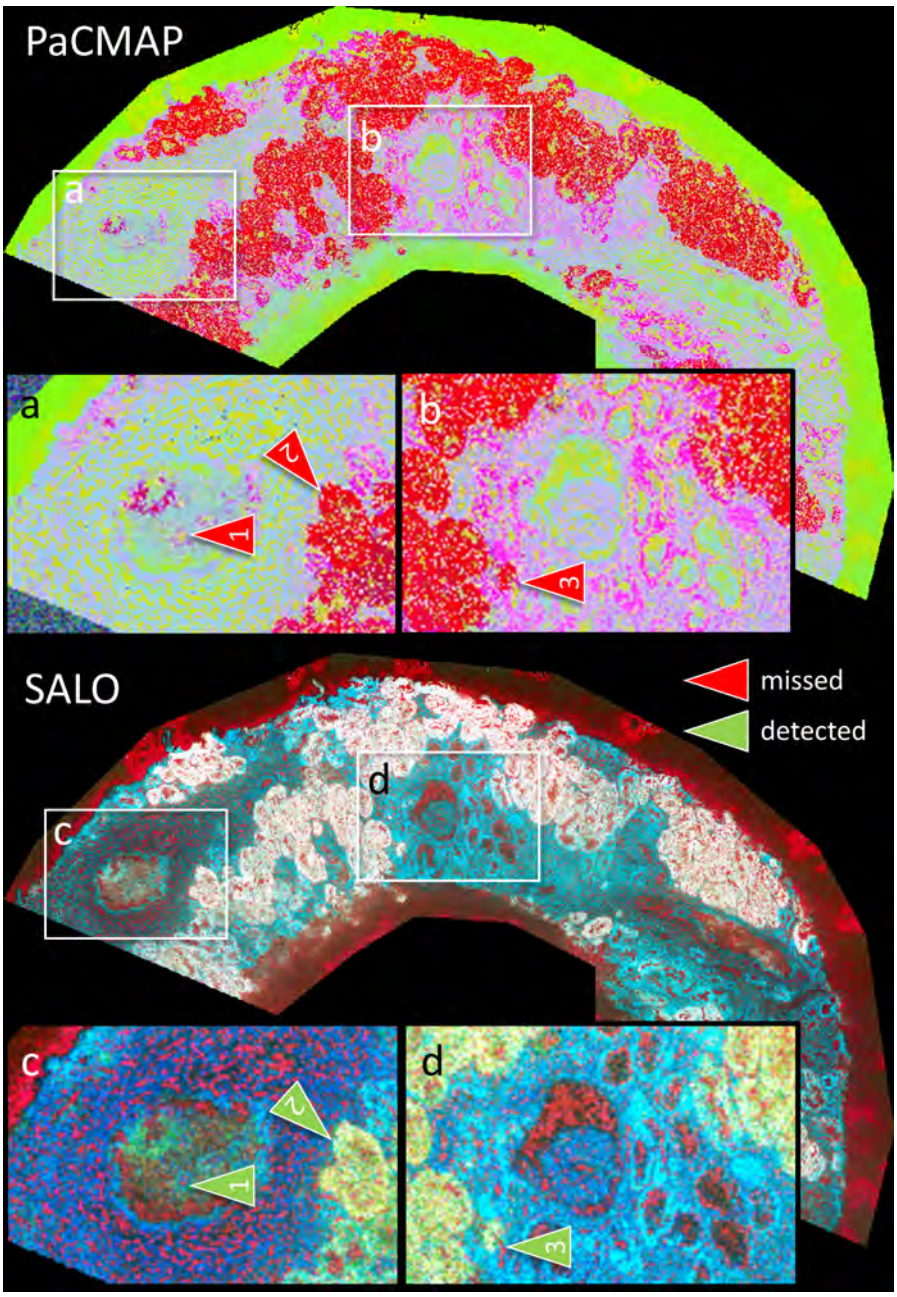

Fig. 3 Human kidney needle biopsy with extensive nephritis/glomerulonephritis (5 μm/pixel resolution). SALO visualization is generally clearer in revealing the organ structure than previous methods. **a-d** show two examples of glomeruli for the improved PaCMAP method (a,b) and SALO visualization (c,d). The arrows indicate examples that are better detectable in SALO: 1) inflammatory cells in **a,c** a glomerulum capillary, 2) proximal tubulus vs. distal tubulus in **a,c**, 3) inflammatory cells (lymphocytes) in a tubulus in **b,d**.

ii) Detecting small structural details in pre-defined anatomical regions:

For research on disease pathomechanisms and treatment development, the detection of subtle anatomical or functional details within known anatomical regions is of exceptional importance. Figure 4a demonstrates an example of the advantages of the proposed visualizations to highlight such subtle detail of sub-nuclei of the thalamus using the proposed visualizations. Small thalamic nuclei are especially pronounced using SALO and TOP3 visualizations. SALO was used to annotate examples of thalamic sub-nuclei (dotted lines, arrows). The annotation mask was then overlaid with the other visualizations to enable comparisons and orientation within the thalamus region. UMAP shows much reduced detail within the thalamus annotation mask. PR3D and TOP3 reveal some but not all thalamic nuclei.

Another example of much-increased detail richness is seen in Figure 4b. It demonstrates the sub-regions or functional domains of the Substantia nigra (SN). Several SN sub-regions representing functional subdomains can be detected visually using the proposed visualizations. Using UMAP for DR these sub-regions aren't detectable at all. Here, we only detect a homogeneous dark blue area, whereas the new visualizations enable the clear detection of sub-regions. For comparison, we included a panel of visualizations and K-means segmentations in the Supplementary Information, Figure 13.

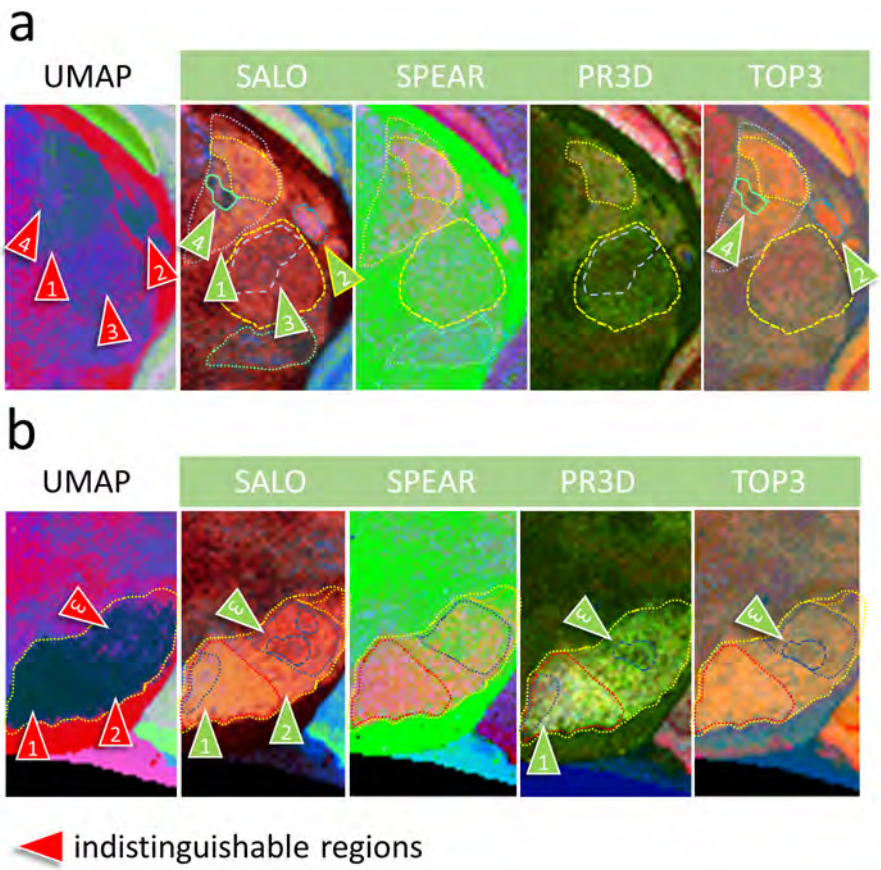

Fig. 4 Improved detection of sub-nuclei in mouse brains. **a** Improved detection of thalamus nuclei. Our proposed SALO and TOP3 reveal more sub-region details in the annotations compared to UMAP. UMAP shows a homogeneous area inside the thalamus region. The red arrows point to the thalamus nuclei that are not distinguishable in UMAP, but in SALO we can identify and annotate them. **b** Substantia nigra (SN) sub-regions can be detected using the new visualizations, where UMAP only shows a homogeneous area. The green arrows point to examples of sub-regions detectable in SALO, SPEAR, PR3D, and TOP3. Green arrows show detection, red arrows show no detection.

iii) Detecting functional details of hippocampal neuronal connections:

We also wanted to assess the ability of the proposed visualizations to reveal hidden functional details in mouse brains, e.g., hippocampal interconnections between neuronal groups. In contrast to the circumscribed, pathological Aβ plaques, these physiological structures consist of connections, neuronal cell bodies, and a few intercalated glia cells, and may not appear as pronounced due to similar m/z content resulting from their close geometrical interactions. Figure 5 and Supplementary Information, Figures 25, 26, show overviews and zoomed-in images of UMAP, SALO, SPEAR, PR3D, and TOP3 visualizations, revealing different levels of anatomical detail of the hippocampal connections related to global data structure preservation in comparison to conventional H&E and immunohistochemical stains (IHC). Such visualization panels can be used

to discover new regions beyond known anatomical annotations, revealing important subanatomical structures for disease research and treatment evaluation.

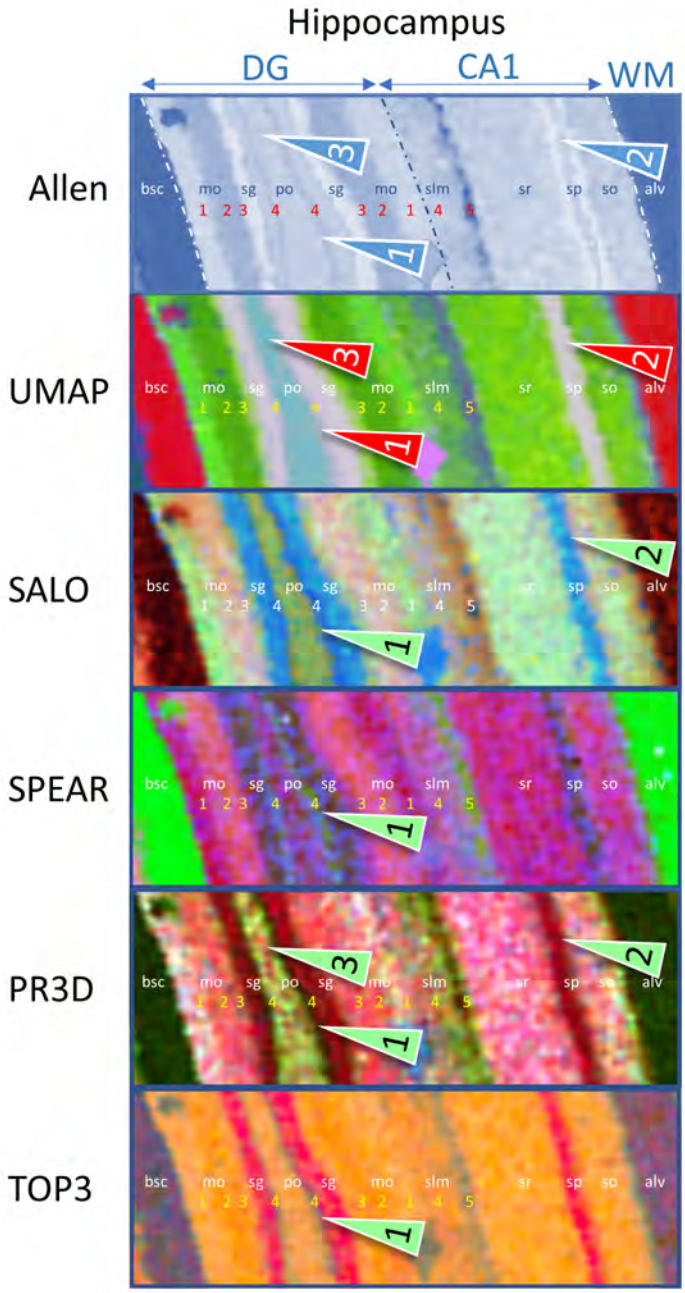

Fig. 5 Using a panel of UMAP, SALO, SPEAR, PR3D, and TOP3 visualizations, different details of the hippocampus formation can be discovered. The Allen brain atlas scheme shows the annotated anatomical structures in blue. The red numbers (1-5) highlight structures that become visible using MSI-VISUAL, but are not annotated in the Allen atlas. These regions represent areas that exhibit a unique lipid content and can therefore be visualized only using MSI lipidomics. The bands of the neuron cell bodies are DG-sg and CA1-sp. The other regions (DG-mo, DG-po, CA1-slm, CA1-sr, and CA1-so) are the different parts of the dendrite and axonal trees of the neurons. Each visualization shows specific parts of the DG-CA1 structure with PR3D and SALO revealing most details. The SPEAR visualization shows a light green color in the white matter (WM) connections, also allowing the identification of the non-annotated areas 4 and 5 as myelin-rich connections. The green arrow 1 highlights a layer of connections below the dentate gyrus neuron cell bodies (DG-sg). The green arrow 2 highlights the CA1 band of neuron bodies (DG-sp). The green arrow 3 highlights the cells of the dentate gyrus in the polymorph region (DG-po). Legend: red arrows - no detection; CA1 - cornu ammonis 1, DG - dentate gyrus, WM - white matter, bsc - brachium of the superior colliculus; DG: mo - molecular layer, sg - granular cell layer (neuron band), po - polymorph layer; CA1: slm - stratum lacunosum moleculare, sr - stratum radiatum, sp - pyramidal layer (neurons), so - stratum oriens; alv - alveus and external capsule.

iv) Detecting single neurons:

The detection of single cells, e.g., giant α motor neurons in the anterior horn of the spinal cord's grey matter, is further explained in the interactive mapping section 5.

Interactive m/z mapping on biological examples using MSI-VISUAL

Determining the spatial distribution of m/z values of metabolites, lipids, and peptides specific for model organisms, anatomical regions, experimental outcomes, etc., is an important task in research. Furthermore, disease-related m/z values could be used as diagnostic markers but also for treatment stratification, e.g., MSI profiles of different cancer subtypes.

To test the general application of MSI-VISUAL to map m/z values on different biological samples with different m/z ranges and spatial resolutions, we analyzed several different cases:

1. Mapping of lipids in anatomical mouse brain regions.
2. Mapping examples from the METASPACE repository: brain tumor and kidney.
3. Mapping human diagnostic brain samples with neuropathological features.
4. Mapping mouse brainstem nuclei and white matter tracts.
5. Mapping single cells: α motor neurons of the spinal cord anterior horn.

1) Mouse brains show region-specific lipid signatures:

Here, we demonstrate the usage of the entire MSI-VISUAL pipeline for fast, interactive mapping of m/z values of different brain regions using a lipid MSI scan of an AD mouse model with pronounced β-amyloidosis [35]. SpecQR examples of the m/z distribution are given in Figure 6. We selected and mapped the cortex, hippocampus, white matter, and brain stem. Each of these regions has a unique lipid signature. The top 5 m/z values are displayed for every region. We show individual m/z images of detected m/z values for verification. Previous work [41] used registration of MSI to MRI to be able to map m/z values belonging to these brain regions.

Using MSI-VISUAL, we are similarly able to map the brain regions, however, without the need for registration to external data modalities such as MRI or IHC stains. We achieve this almost instantly in a fraction of the time compared to the process proposed by [41], by simply selecting regions in the software. This has implications for diagnostic use or research discovery, where MSI could provide multiple modes of assessing slides simultaneously by delivering a visualization panel of several quantitative, trustworthy visualizations.

We map Aβ plaques simply by selecting them in the MSI-VISUAL viewer. Of note, some m/z values, such as 885.6 Da, highlight the plaques in addition to cortex regions, showing that the Aβ plaques absorb and concentrate these lipids from the cortex. Other m/z values, such as 1179.8 are more unique to cortical plaques and are mostly seen in the hippocampus. This is the first time, m/z values for plaques are determined from within MSI images, in contrast to searching for known, pre-determined, plaque m/z values.

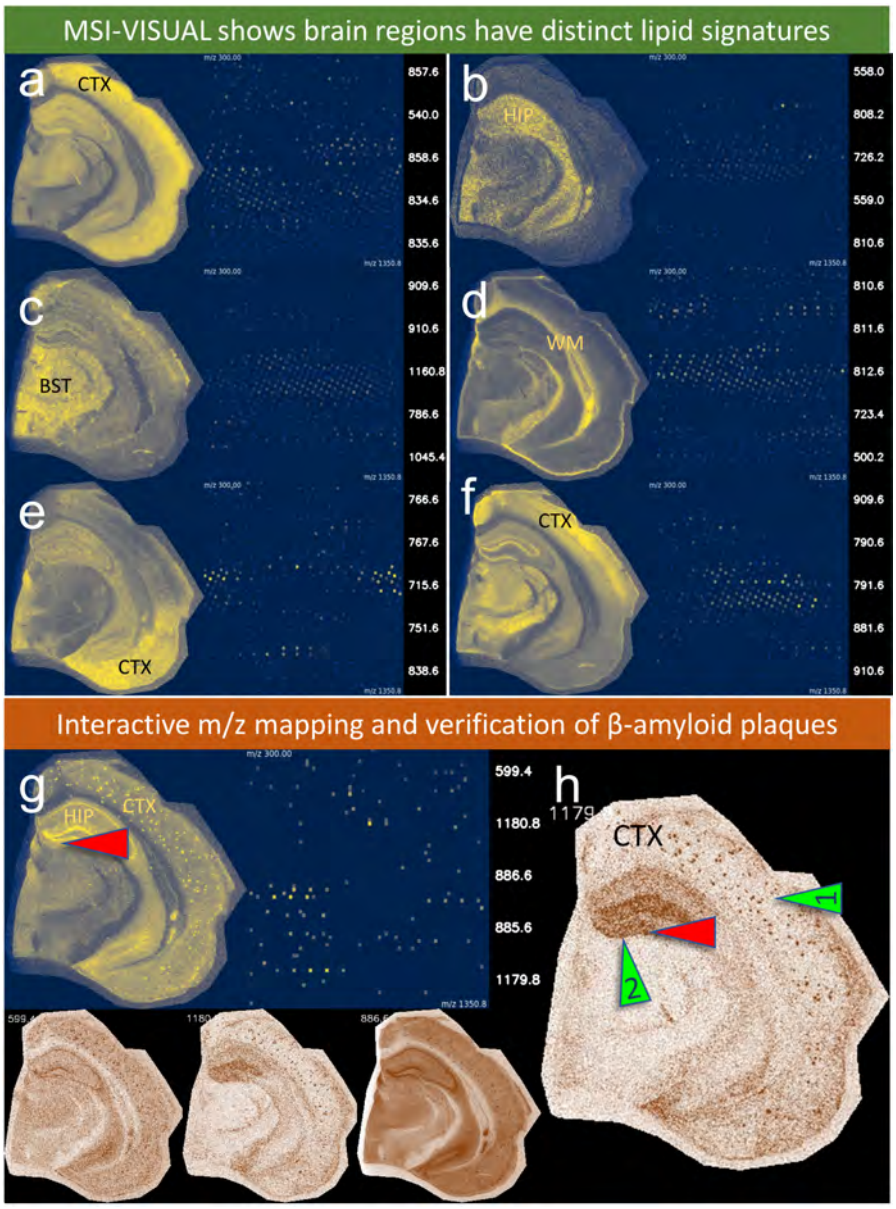

Fig. 6 Interactive mapping of the m/z components of the brain. **a-h** brain lipid MSI scan of an AD mouse model with Aβ plaques. **a-f** ion current summary images and SpecQR graphs selective for **a** the isocortex (CTX), **b** the hippocampus (HIP), **c** the brain stem (BST), **d** white matter (WM), **e** piriform cortex (CTX), and **f** upper isocortex regions (CTX) and connections in the hippocampus and brain stem. **g** Aβ plaques have a distinct lipid m/z signature with 599.4, 885.6, 886.6 (M+1), 1179.8, and 1180.8 (M+1) being the 5 highest m/z values in this example. The SpecQR summary image and the Virtual Pathology Stains (VPS) of the top m/z values are used for verification (in brown). VPS delivers a continuous 'stain' similar to those used for pathology diagnostics. **h** An image with numerous plaques (arrow 1) in the isocortex (CTX), containing the plaque-specific m/z 1179.8 (ganglioside GM3 [36]), which is also found in hippocampal connections (arrow 2). The red arrow depicts an Aβ plaque also labeled in the consecutive H&E-stained section of the frozen tissue block used for MSI (Supplementary Information, Figure 28).

2) Interactive mapping of metabolomics and lipidomics datasets.

To test the general applicability of MSI-VISUAL, we wanted to assess MSI data generated by others freely available on METASPACE [9]. The results for m/z mapping of a human kidney biopsy (lipidomics dataset, m/z 300-1350, 5 μm-resolution) and a mouse brain with implanted brain tumor cells (metabolomics, m/z 50-400, 20 μm-resolution) are shown in Figure 7. These examples show the determination of region-specific m/z values. The kidney needle biopsy of a glomerulonephritis patient nicely highlights its anatomical structures, e.g., glomeruli and tubuli, but also the extensive roads of inflammatory cells and their unique m/z patterns. The brain tumor example highlights tumor-specific metabolites and their m/z values. Both examples show the power MSI has when providing DR-related visualizations.

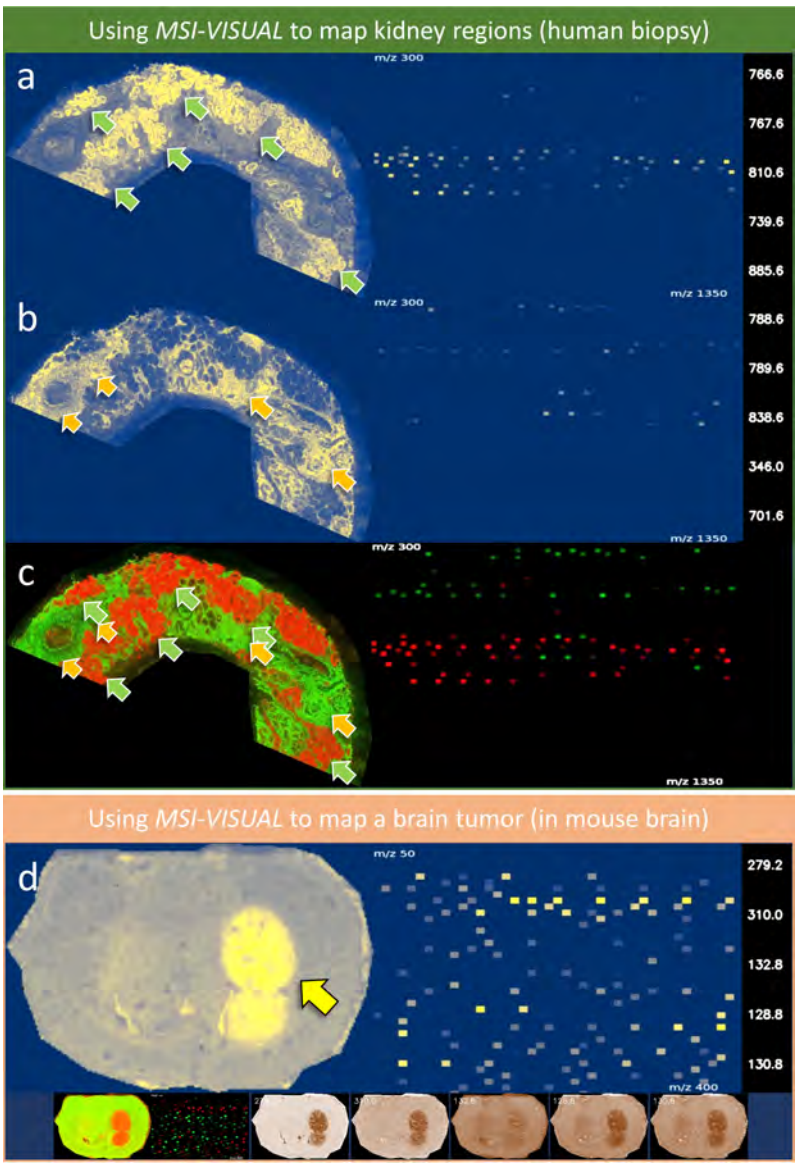

Fig. 7 Mapping metabolomics and lipidomics datasets from the METASPACE repository. **a-c** Mapping lipidomics m/z values 300-1350 of different regions in a human kidney needle biopsy (Table 2, dataset 4), aggregated images of the 5 most specific m/z for **a** the kidney tubuli system (green arrows) and **b** inflammatory cells (orange arrows) around glomeruli and between the tubuli. **c** 2-channel overlay image of tubuli (red) and inflammation (green). The SpecQR nicely presents the separated m/z values (green and red squares). **d** Mapping metabolomics m/z values 50-400 of an implanted brain tumor (yellow arrow) into a mouse brain from [42]. The SpecQR shows the specific metabolite pattern of the lesion. The lower row of images are virtual pathology stains of the 5 most significant m/z values and a differential red-green image of tumor vs other tissue.

3) Interactive mapping to differentiate neuropathological lesions for diagnostics.

Post-mortem human brain tissue of a patient with vessel-related dementia and AD was investigated using peptide MSI [43]. The data have been pre-processed and are peak-selected for the 500 best peaks. We wanted to automatically identify diagnostically relevant neuropathological lesions in these brain sections. The example in Figure 8 shows the identification of Aβ-deposits related to AD and, additionally, the severe capillary leakage related to vascular dementia (VD). We selected the segmented ROIs according to their color (green or red/blue), and MSI-visual generated the output of the 5 most significant m/z values for each ROI. The identification of these specific m/z values enabled the correct identification of the ongoing neuropathological processes and their tissue locations in this mixed dementia case. Similarly, this approach can experimentally be used for the assessment of mouse models for treatment development, e.g., for quantifying the adverse effects of anti-amyloid antibodies.

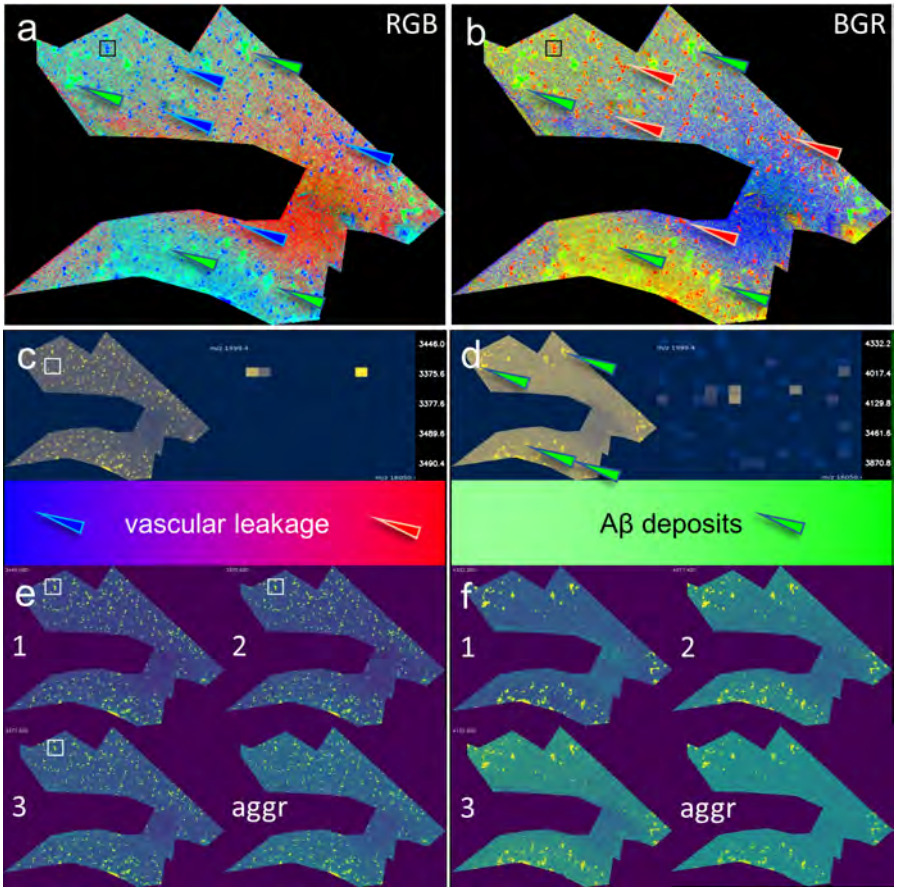

Fig. 8 Visualization and identification of intracerebral lesions to diagnose neuropathological conditions by assessing their specific m/z values. **a,b** NMF visualization (2000 iterations) in 3 color channels (RGB) presented with two different colorizations, RGB and BGR. The box and red/blue arrows mark examples of numerous smaller, partially accumulating/aggregating structures. The green arrows highlight larger, more confluent structures. These structures were selected for m/z mapping and identification of their potential pathological origin. **c** the m/z fingerprints and SpecQRs reveal extensive capillary leakage and **d** larger Aβ depositions with Aβ1–40 (4332.2 Da), Aβ1–38 (4129.8 Da). **e,f** presentations of the three most significant m/z values (1–3) and the aggregated mean images of these three m/z values (aggr). **e** highlights severe capillary leakage as seen in vascular dementia. **f** shows Aβ pathology as seen in Alzheimer's disease. Thus, the neuropathological *post mortem* diagnosis is mixed-type dementia. ProteomeXchange dataset PXD049325, peak-selected, peptide MSI, case S2-SAD provided by [43].

4) Mapping of brain nuclei and white matter tracts:

As an additional example, MSI-VISUAL facilitates the identification and characterization of functional groups of neurons (nuclei) and their connections (white matter tracts). The interactive visualizations enable the mapping of specific m/z values of the selected brain structures, providing high functional resolution, as demonstrated

for hippocampus neurons and their connections (Figure 9 and Supplementary Information, Figure 27). The TOP3 method revealed structures such as the substantia nigra (SN) and cerebral peduncle (cpd), which were used as ROIs for m/z comparison. ROI1 (substantia nigra) was characterized by its neuronal content and connections, while ROI2 (cerebral peduncle) presented as white matter. The m/z values in ROI1 also correspond to areas rich in neuronal content, such as the hippocampus and its connections. ROI2 was correctly identified as a white matter tract, with no overlap in m/z values between the grey and white matter regions. The ion images and SpecQR graphs confirmed these distinct m/z distributions.

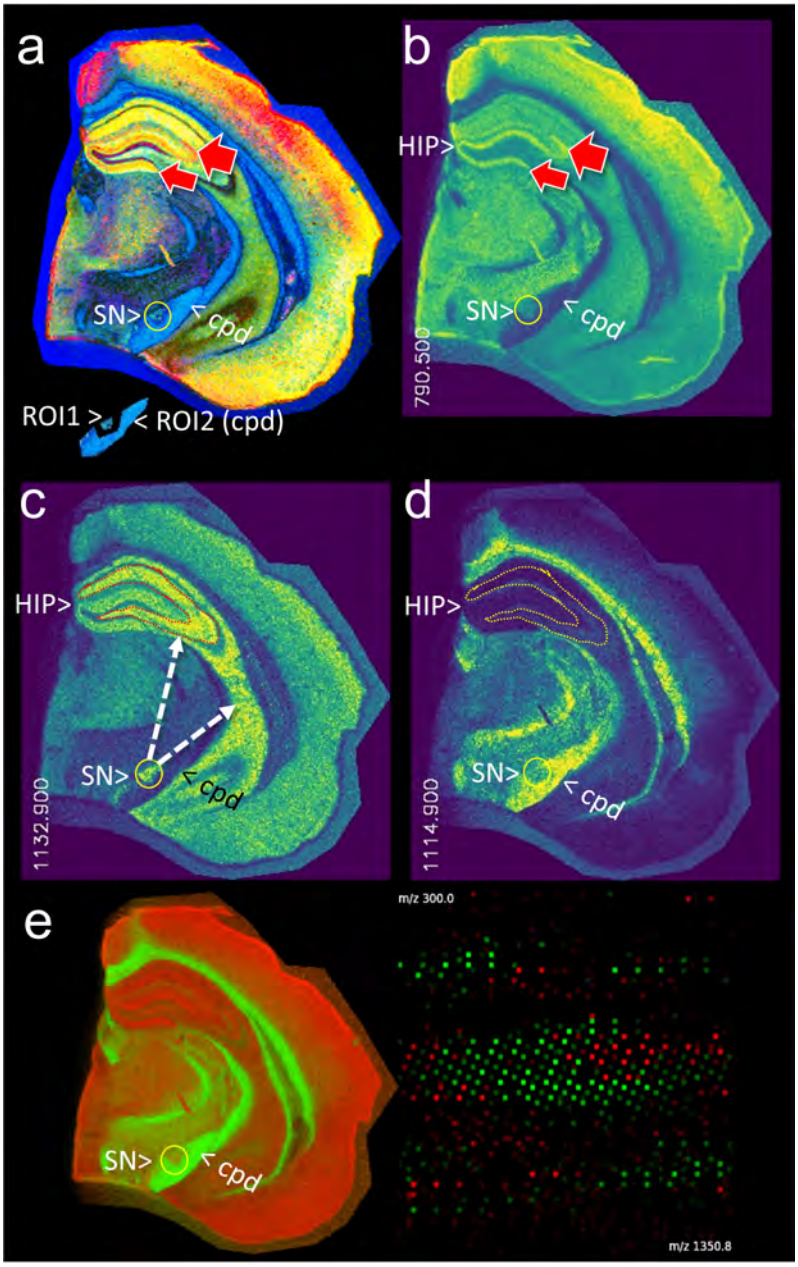

Fig. 9 Determination of m/z values, specific for anatomical and functional brain regions. **a** TOP3 visualization reveals detailed brain structures, including ROI1 (Substantia nigra, SN) and ROI2 (cerebral peduncle, cpd). **b,c** ROI1 (SN) was identified as a neuronal region, with m/z values corresponding to other high-density neuronal regions such as the hippocampus (HIP). **d** ROI2 (cpd) was correctly identified as a white matter tract, with no overlap with the SN. **e** Overlay of the top five m/z values from ROI1 (red) and ROI2 (green), with SpecQR graph showing the m/z distribution from 300–1350, confirming distinct m/z profiles of grey substance (red) and white matter tracts (light green).

5) Mapping m/z values of large neurons in the spinal cord (single-cell mapping):

We wanted to assess the possibility of detecting and analyzing single cells. As an favourable example, we chose the giant spinal cord αMNs, which are located in the gray matter of the anterior horn. Recently, Gruber et al. [44] presented fast, label-free quantum cascade laser mid-infrared imaging microscopy (QCL-MIR imaging) to guide MSI to high-interest tissue regions, such as kidney glomeruli, cultured multicellular spheroid cores, and even single motor neurons in the spinal cord of mice. More than a decade ago, Hanrieder et al. [45] also analyzed these spinal motor neurons using Time-of-Flight Secondary Ion Mass Spectrometry (ToF-SIMS). Therefore, we wanted to evaluate our computational approach using MSI slides with 5 μm spatial resolution (Table 2, dataset 5) as shown in Figure 10. αMNs are one of the largest nervous system cells in the human body with a diameter of 40-70 μm and an area of 1000-2000 μm^2, covering > 100 pixels in this example (Figure 10g). We employed a digital selection step for a cellular ROI (repeated 3 times) to be able to assess the molecular profile of these single αMN vs. the surrounding spinal cord tissue. Each time, the diagram showed signal enrichment in the αMNs and partially in the surrounding grey matter of the spinal cord. The selection was guided to be negative in the spinal cord's white matter (myelin). The mapped m/z values can be used to confirm the cell entity [44] and to evaluate changes during disease processes, e.g., in amyotrophic lateral sclerosis (ALS), a neurodegenerative disease involving the first (in the brain's motor cortex) and second (in the spinal cord) motor neurons.

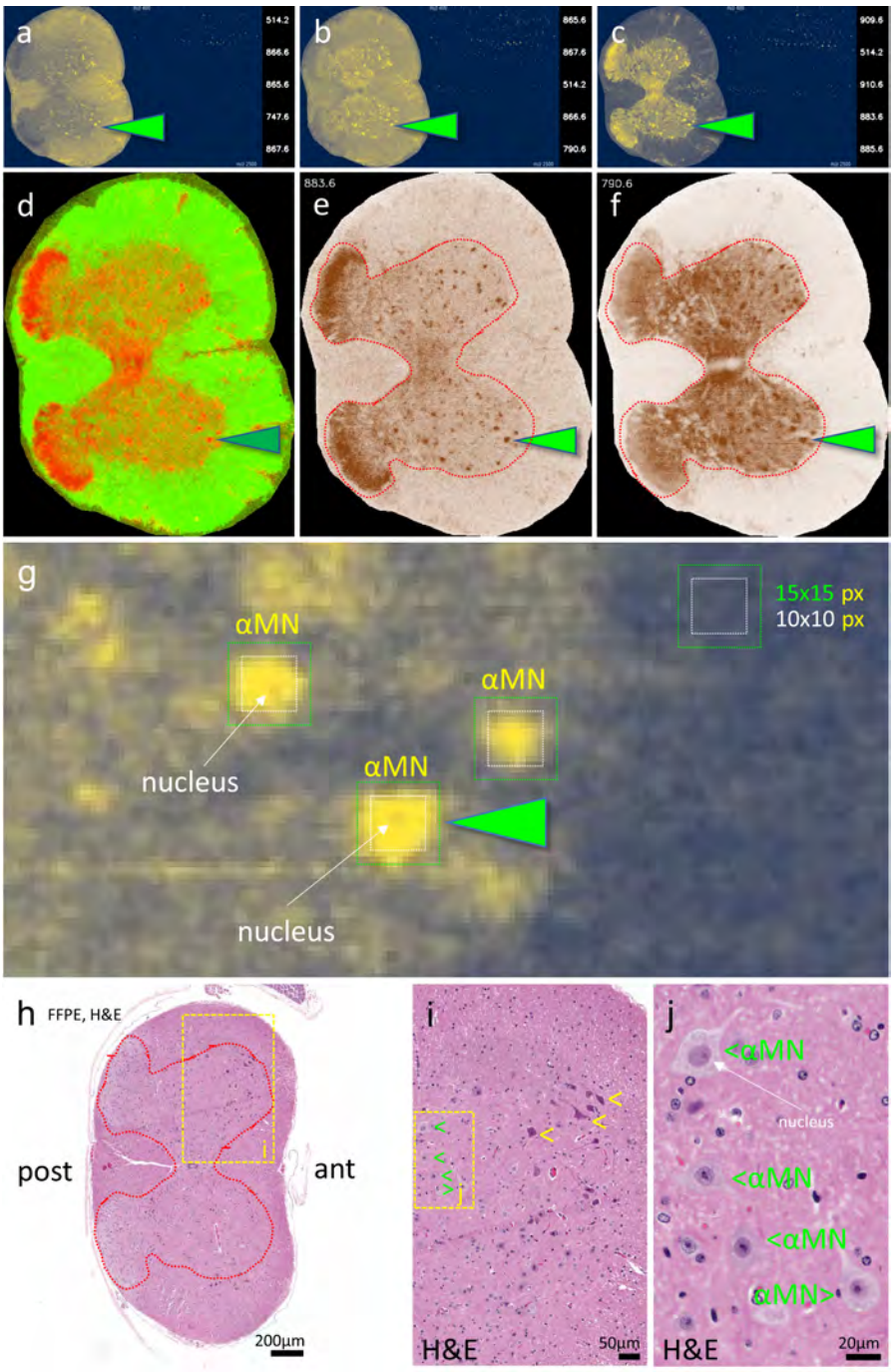

Fig. 10 Example of the detection of single neurons — spinal cord α motor neurons (αMNs) — using MSI with 5 μm/pixel resolution. **a-c** show three independent rounds of interactive ROI selection for putative αMNs, the calculated specific m/z values (list on the right), and SpecQR graphs (middle). Fresh frozen tissue was used to perform MSI (dataset from METASPACE, Table 2, dataset 5). **c** best performing ROI selection (pixel-wise) showing the 5 best m/z values as an aggregated ion image. Two of the significant m/z values highlight phosphoinositols PI (18:0/20:4) 883,548 Da and PI (18:0/22:6) 885,564 Da, and have been described recently in aMN [44]. **d** shows a red-green overlay image to highlight the αMNs (second motor neuron affected in amyotrophic lateral sclerosis (ALS)) and their posterior horn connections (red channel). The surrounding white matter regions of the myelinated spinocerebral and cerebrospinal tracts are colored in light green. **e,f** show two Virtual Pathology Stains (VPS) of specific m/z examples (883.6 and 790.6). The red dotted line delineates the grey substance of the spinal cord with the central aqueductus. **g** shows a zoomed-in of **c** to assess the number of pixels covered by the αMNs. The green arrows point to an example covering > 100 pixels. Confident assessment of single cells in MSI is feasible if at least 3x3 pixels are covered by the structure. **h** A routine pathology H&E overview of a mouse spinal cord section from formalin-fixed, paraffin-embedded (FFPE) mouse tissue. The FFPE sections are slightly shrunken due to extensive pretreatment procedures (dehydration, delipidation, paraffinization). The MSI sections from METASPACE presented in **a-g** were made from fresh-frozen tissue. **i** magnification of the anterior horn highlighting αMNs. The green arrows point to healthy neurons, the yellow arrows point to αMNs artificially changed (condensed cytoplasm and shrunken cell body) during the harvesting procedure. **j** high magnification of four αMNs. The white arrow points to the nucleus. ant - anterior, post - posterior.

Biological interpretation of mapped m/z values by MSI-VISUAL

For the neurobiological experimentalists, we present two examples demonstrating how MSI-VISUAL facilitates biological insights through the visualization of mapped m/z values. Here, we stress that for the sole visualization of MSI data, it is not necessary to analyze full resolution m/z values in the first place; it is rather advised to bin the data appropriately depending on the m/z range and the number of features. Without binning, the size of the internal files may easily exceed the available RAM. Here, TOP3 and PR3D visualizations demand less computational power and allow for fast and reliable screening of the tissue structure. The mapping process is enabled by the entire pipeline: the visualization panel reveals sub-regions, which can then be interactively investigated using the m/z mapping functionalities of MSI-VISUAL.

Figure 11 illustrates the identification of a lipid that is enriched in a sub-region of the Substantia nigra (SN) in an ABCA7-deficient mouse (A7ko) [35], highlighting the localized effects of ABCA7 loss. To explore region-specific lipid differences, we compared UMAP and SALO visualizations for mapping m/z values across brain sub-regions. While SALO successfully distinguished two sub-regions within a selected region of interest (ROI1), UMAP failed to resolve these differences. Within ROI1, we identified m/z 722.6 Da, which was strongly enriched in this region. A second m/z 885.6 Da exhibited a weaker, though noticeable, preference for ROI1. The m/z 722.6 lipid, detected in negative mode, is a candidate for several lipid species, including phosphatidylethanolamine (PE 34:1), phosphatidylserine (PS 32:0), and ceramide (Cer 42:2;O3 [M+OAc]-).

Figure 12 demonstrates the determination of m/z values associated with Aβ plaques. To investigate the lipid composition within these plaques, we examined the spatial distribution of m/z 885.6 (PI 38:4) using MSI-VISUAL. This lipid, known to be abundant in neuronal connections in the brain [46, 47], was also detected by us in spinal cord neurons. When comparing visualization methods, TOP3 successfully highlighted numerous Aβ plaques, while UMAP failed to resolve them.

Further analysis using SpecQR diagrams of both the spinal cord and brain revealed that several m/z values were shared between spinal cord neurons and cortical Aβ plaques. Ion images of m/z 885.6 in two AD mouse models revealed its presence in large spinal neurons, Aβ plaques, and hippocampal neuronal connections. These findings suggest that m/z 885.6 is a physiological component of neuronal structures and accumulates, therefore in Aβ plaques, likely due to the degradation of neuronal connections within these pathological structures.

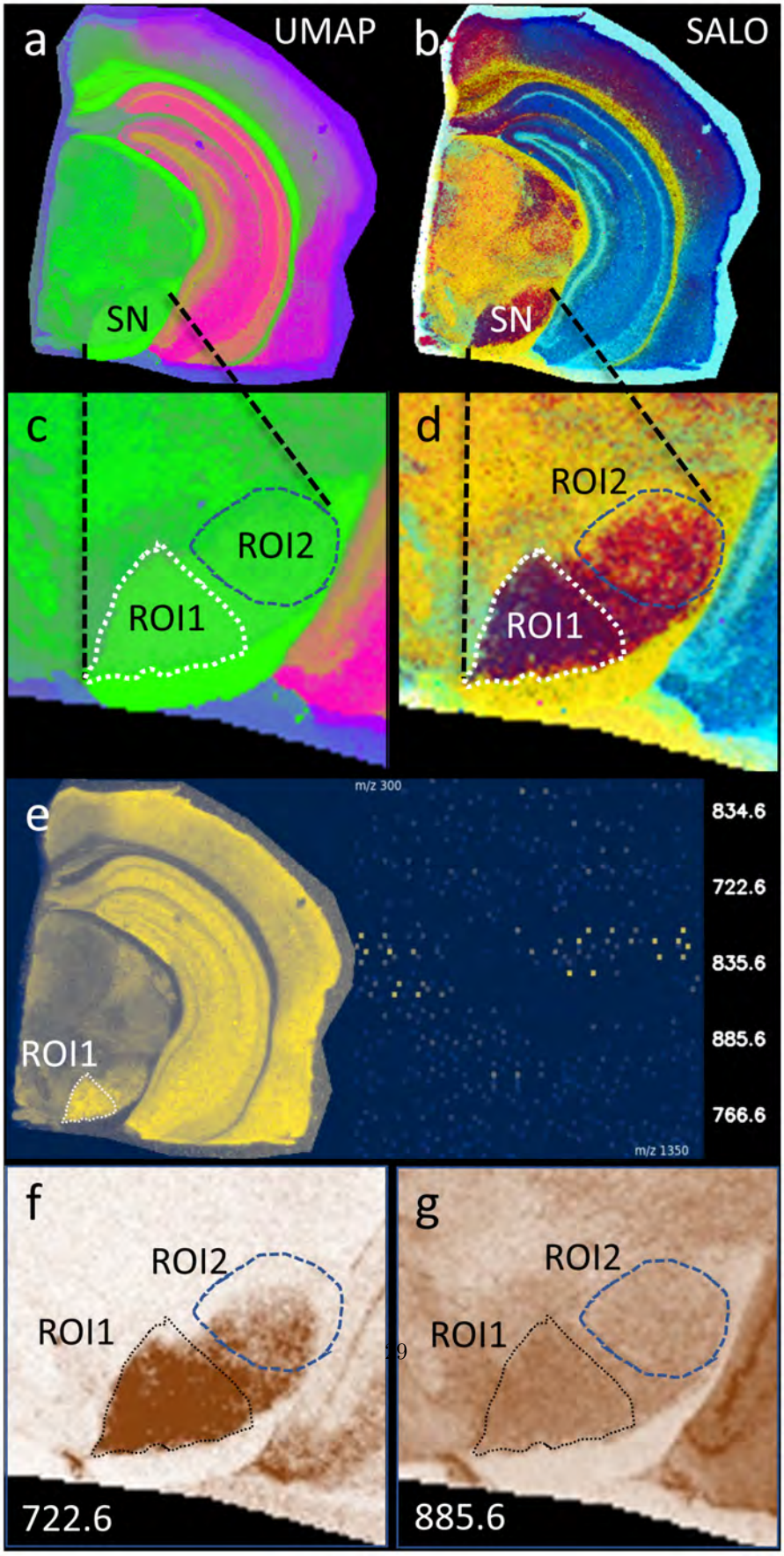

Fig. 11 Index lipids mark region-specific neuronal differences in an ABCA7-knockout mouse. **a,c** UMAP visualization, **b,d** SALO visualization identified two distinct sub-regions (ROI 1,2) within the Substantia nigra (SN), which were not resolved by UMAP. **e** The mapping analysis reveals the five most significant m/z values. The Virtual Pathology Stain and the SpecQR show the distribution of the m/z values. **f** m/z 722.6 is strongly enriched in ROI1. **g** m/z 885.6 is only slightly increased in ROI1.

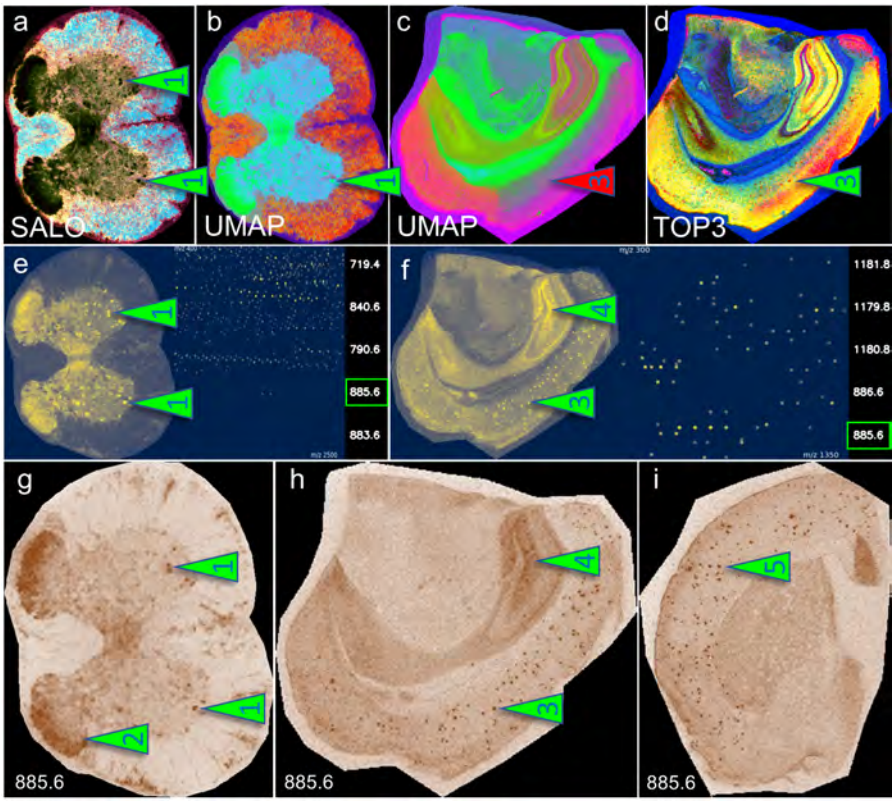

Fig. 12 MSI-VISUAL's m/z mapping function reveals shared lipid content in spinal cord α motor neurons and cortical Aβ plaques. **a-d** Visualizations of spinal neurons (arrows 1) and Aβ plaques (arrows 3). **c** UMAP does not highlight plaques (red arrow 3). **d** TOP3 successfully detects plaques. **e-f** the aggregated ion image and SpecQR diagrams show m/z values shared between spinal neurons and cortical Aβ plaques (green box). **g-i** Virtual Pathology Stain images of m/z 885.6 - PI(18:0/22:6) - in the spinal cord neurons [44], and brains of two AD mice. **g** spinal cord anterior horn α motor neurons (arrow 1) and hind horn connections (arrow 2). **h** hippocampal connections (Dentate gyrus' molecular layer, arrow 4). **h,i** cortical Aβ plaques (arrow 3 and 5).

Discussion

Mass Spectrometry Imaging (MSI) can be a valuable tool for research and tissue diagnostics if the resulting large datasets are presented using appropriate high-fidelity visualizations to reveal sufficient detail of the internal tissue structures or their functional deficits.

Here, dimensionality reduction (DR) plays an important role in preserving the global data structure of MSI data. Our proposed DR methods can be used to generate highly informative images with continuous color gradients in the RGB space, similar to histological slides used in surgical pathology, stained with specific color or enzyme stains, or immunohistochemical (IHC) methods. Panels of such visualizations and specific virtual pathology stains (VPS), mimicking IHC stains, could be used for on-the-fly pathology diagnostics.

The current MSI convention is to use the alignment of MSI data with additional histological stains for ROI identification, relying on known histological features [5]. However, continuous color gradient images and m/z mapping are prerequisites for the wider diagnostic implementation of MSI techniques in pathology, similar to immunohistochemical stains. For experimental researchers, the details of differences in selected ROIs are coded in intensity and colorization and can be used together with m/z mapping, e.g., as SpecQR, to assess differences between experimental groups.

Our results demonstrate that both SALO and SPEAR consistently outperform other visualization methods across the two benchmarked datasets. SALO notably performs better than all previously published methods on all images individually. Compared to UMAP [16, 17], SALO improves by a large margin (approx. 0.3 and 0.4 for UMAP on both datasets and above 0.8 for SALO). The low performance of UMAP means that UMAP should be used with caution in MSI, potentially measuring its performance when applied. SALO also improves upon PaCMAP [27], which was created to improve UMAP's global structure preservation, and upon PCA [21], a classic gold standard method for this. As noted in the introduction, we attribute this to the direct optimization of global structure in SALO compared to the indirect optimization used in PaCMAP, and to the complex non-linear transformation we used compared to the linear projection used by PCA. SALO and SPEAR also demonstrate their utility in combining different distance functions, resulting in robustness to both distance functions—another need in MSI, as discussed in our introduction and noted previously in [17, 19].

In contrast, TOP3 is surprisingly competitive despite its simplicity. While TOP3 performs better than UMAP [16] even with different binning, it does not achieve the same level of performance as SALO and SPEAR. Despite this, TOP3 stands out due to its low computational requirements, positioning it as a practical tool for MSI analysis, particularly in resource-constrained environments where methods such as SALO or UMAP are unable to run. Notably, because TOP3 operates on pixels independently, a future optimization could enable partial loading of MSI data, allowing for the visualization of image blocks without requiring the entire dataset to be loaded at once.

The PR3D visualization, however, did not perform well on all METASPACE datasets. This outcome was partially anticipated, as the hyperparameters for PR3D were specifically tuned for the mouse brain dataset. Future work will focus on developing methods for the fast, automatic selection of optimal PR3D parameters to enhance its performance across different datasets.

The following limitations of our study must be acknowledged. Although our visualizations emphasize high global structure preservation and reveal anatomical details that assist in annotation, local structure preservation was not the primary focus of this study. For instance, in the case of the TOP3 visualization, unrelated regions are assigned the same color (e.g., red), which can compromise local structure preservation. Addressing local structure preservation in MSI and its use cases is a potential avenue for future research. Another limitation of our SALO and SPEAR visualizations — though not of TOP3 or PR3D — is the lack of color consistency across images. The resulting RGB colors can vary depending on the random seed and the set of sampled reference points for advanced visualizations. For example, the cortex may appear red in one visualization and green in another. This is a general technical limitation of non-parametric DR methods, which do not provide a fixed mapping across datasets. Overcoming this limitation is an important direction for future research. One approach could involve training parametric models to approximate the output of these methods, allowing for consistent application across images. Alternatively, consistency constraints could be incorporated directly into the optimization process to stabilize the color assignments across runs and datasets.

Another limitation of our visualization benchmarking is that, for all methods, we use the default hyperparameters (excluding UMAP, for which we applied it twice with different distance functions). It is possible that searching for optimal hyperparameters for the specific benchmarks would improve their performance, as well as the performance of our methods; although it is not practical, we expect visualizations to be created with a single set of parameters in most cases. Since this is extremely computationally intensive, we will leave this for future studies.

We also anticipate potential improvements for SALO. A major limitation is its reliance on a fixed set of reference points. While re-sampling these reference points could enhance the visualizations, it may come at the cost of increased convergence time and higher computational expenses. Thus, future work will explore ways to balance performance improvements with computational efficiency.

Another often proposed challenge for visualizations is the possible dependence on data extracted using fixed bins and the summation of m/z values within those bins. Binning is widely used for MSI data pre-processing [12, 13, 48]. Extracting m/z values with higher precision thus requires the use of a larger number of bins and significantly more computational requirements. The memory constraints are a major bottleneck for advanced truthful visualization techniques, e.g., requiring $> 256GB$ RAM for a single mouse brain hemisphere in our tests. Although this approach is standard in MSI, future advancements could explore strategies to optimize or even eliminate the need for binning.

Here, it is highly important to distinguish between truthful visualizations and m/z identification with igh precision: our proposed visualization methods perform well and

reveal highly detailed anatomical structures, even with binned m/z data. Our tests of a brain hemisphere with 5, 10, and 20 bins showed no substantial visualization differences for advanced techniques, e.g., UMAP; but 5 bins generated even better visualizations for the lightweight methods PR3D and TOP3 (Supplementary Information, Figure 16). Using another dataset, it even appeared that our lightweight method, TOP3, and the new advanced methods, SALO and SPEAR, are robust against binning (Supplementary Information, Figure 17). Thus, binning is routinely interpreted as a problem, but it should rather be regarded as even improving DR visualizations. We strongly suggest assessing the effects of binning for each dataset and DR method separately.

However, for precise mass identification - which lies beyond the scope of this work - full m/z resolution would be beneficial. Here, we can suggest using visualizations with binned spectral data for annotating fine-grained ROIs or single cells, and then using, e.g., Gaussian Mixed Models (GMM) for high-resolution m/z extraction [38, 48].

Finally, MSI-VISUAL provides a rapid and interactive platform for mapping and exploring MSI data, as illustrated in the biological examples section. By utilizing MSI-VISUAL, we were able to identify and select sub-regions within our visualizations and perform efficient m/z mapping, revealing new biological insights into the shared lipid content of neurons, plaques, and substantia nigra sub-regions. These capabilities underscore the potential of the new visualizations for applications that demand fast results, such as clinical diagnostics or research settings requiring swift exploration of MSI data. MSI-VISUAL was practically tested, establishing a high-resolution computational lipid brain atlas consisting of 124 annotated mouse brain regions [38].

Methods

The lipidomics MSI mouse brain dataset.

The mouse brain MSI data files were generated using frozen hemispheres from four 100-day-old animals (C57Bl/6J genomic background). Two mice expressed combined human mutated APP and PS1-mutated transgenes (APPtg) for the generation of Aβ plaques [34, 40, 49]. Frozen mouse hemispheres were coronary cut into 10 μm-thick sections using a cryomicrotome (CM1950, Leica, Nussloch, Germany) and placed on a single Intellislide (Bruker Daltonics, Bremen, Germany). The section was dried in a vacuum chamber and sprayed with N-(1-Naphthyl) ethylenediamine dihydrochloride (NEDC) matrix dissolved to 7 mg/ml in 70% methanol using an HTX3+ TM Sprayer (HTX technologies, Carrboro, NC, USA) as described by Andersen et al. [50]. Matrix-assisted laser desorption ionization trapped ion mobility mass spectrometry imaging (MALDI-TIMS-MSI) was performed in negative mode using a timsTOF fleX™ mass spectrometer (Bruker Daltonics, Bremen, Germany). Mass calibration was performed using red phosphorus and ion mobility using ESI-L Low Concentration Tuning Mix (Agilent Technologies, Santa Clara, CA, USA) in ESI mode. For MALDI-TIMS-MSI analysis, a mass range of m/z 300 – 1350 and a range of the inverse reduced mobility (1/K0) of 0.7–1.8 Vs/cm^2 was used. The laser was operated at a frequency of 10 kHz with a burst of 200 shots per pixel with a spatial resolution of 20 μm. Four mouse hemispheres were assessed in a single overnight run (Supplementary Information, Table 1). The mouse brain lipidomics dataset files are available at the ProteomeXchange PRIDE repository with the dataset number PXD056609.

The human proteomics MSI dataset.

The human brain MSI data files have been downloaded from the ProteomeXchange PRIDE repository with the access code: PXD049325 [43].

Open-access metabolomics and lipidomics datasets.

The METASPACE datasets used for the benchmarking and testing are listed in Supplementary Information, Table 2.

Data extraction and pre/post-processing information.

For the extraction and binning of the mouse brain dataset, we used the "extract_bruker_tims.py" script from MSI-VISUAL. For the extraction and binning of the slides from METASPACE, we used the "extract_pymzml.py" from MSI-VISUAL. Binning can be adjusted to the needs of the user and the available computational power needed for the later visualizations. We evaluated 5, 10, and 20 bins per m/z (respectively $0.2 = 200mDa$, $0.1 = 100mDa$, and $0.05 = 50mDa$ precision). During the extraction, m/z values are rounded to their closest bin and are summed there. Binning with 5 bins showed the best visualization results with the light-weight visualizations PR3D and TOP3 compared to 20 bins; highly resource-dependent visualizations, e.g., UMAP, did not show significant visualization differences between 5, 10, and 20 bins

(Supplementary Information, Figure 16). Thus, the presented results were generated using 5 bins. When creating the visualizations, we use TIC [51] normalization, which divides the intensity of each m/z by the sum of the intensities for that pixel. In all visualizations, we use outlier clipping and clip the 0.01 and 99.99 percentiles of the data, also known as Winsorizing [52].

Visualization methods

Motivation for the saliency metric used in SALO. We first outline the motivation behind the saliency metric used in SALO. This metric serves as an objective function for optimization but can also be used to evaluate MSI visualizations. An effective saliency metric should satisfy the following key properties:

- **Preservation of important details.** Pairs of points that exhibit large distances in the input space but are mapped to small distances in the visualization should be penalized. This ensures that meaningful structural differences are preserved.
- **Higher weight for rare but significant differences.** Pairs of points with large distances in the input space should have a greater influence on the saliency score. While such pairs may constitute a small fraction of the total, they are critical for salience. Without this weighting, structures comprising a small percentage (e.g., $< 1\%$) of all pairs might be completely overlooked; yet, the overall metric could still appear high. Additionally, points with very small input-space distances can artificially inflate the saliency score, despite not contributing to meaningful structure identification.
- **Integration of Cosine and L_∞ distances.** The metric should accommodate multiple distance functions to capture diverse biological structures. Some structures manifest themselves through a few distinct m/z values with large intensity changes (better captured by the distance L_∞, while others involve coordinated changes across many m/z values with smaller individual intensity variations (better captured by the distance of Cosine). Both types of patterns should be detected.
- **Incorporation of perceptual color differences.** The metric should account for human perceptual biases in color interpretation. For instance, subtle variations in shades of pink may be difficult to distinguish, even if the visualization encodes meaningful numerical differences. A saliency metric that aligns with human visual perception ensures that the detected structures are recognizable to users.

The Saliency objective definition. For each pair i, we compute its ranking among the other Cosine and L_∞ distances and take the larger ranking:

$$R_{\max}(X_i) = \max(R_{\text{cosine},i}, R_{L_\infty,i})$$

This ensures that property 3 is satisfied. Converting raw distance values to ranks enables us to compare values from different distance functions and directly relate input distances to output distances. For the output, we measure the L_2 distance in the visualization space, specifically in the LAB color space, to account for perceptual differences (satisfying property 4). We then compute the rank $R(Y_{\text{LAB},i})$ of each pair in this color space. We define Δ-saliency for each pair of points i as the ability of the

visualization to rank the output at least as high as the input, with a tolerance of Δ (satisfying property 1):

$$\Delta\text{-saliency}_i = \sigma_\Delta(i) = \mathbb{I}\left(R(Y_{\text{LAB},i}) - R_{\max}(X_i) + \Delta > 0\right) = \begin{cases} 1, & \text{if } R(Y_{\text{LAB},i}) - R_{\max}(X_i) + \Delta > 0 \\ 0, & \text{otherwise} \end{cases}$$

The overall Δ-saliency is computed as the weighted average of $\sigma_\Delta(i)$ across all point pairs, where the weights are determined by their ranks (ensuring property 2):

$$\Delta\text{-saliency} = \sum_i \frac{\sigma_\Delta(i) \cdot R_{\max}(X_i)^\gamma}{\sum_i R_{\max}(X_i)^\gamma}$$

Finally, we define the **Average Saliency** as the mean of the Δ-saliency values for $\Delta = 10\%$, 20%, and 30%.

Saliency Optimization. We approximate the Saliency metric, and then optimize for a visualization that maximizes it with stochastic gradient descent (SGD). We approximate Δ-saliency by sampling fixed reference points to reduce the number of pairs from being quadratic with the number of pixels. SALO optimizes over the set P, all pairs of each image point, and all the reference points:

$$P = \{(a, b) \mid a \in \text{Image}, b \in \text{Reference points}\}$$

The average Saliency metric defined above as the sum over all image pairs is then instead restricted to the set of pairs P. The ranking is not differentiable. Therefore, we use soft ranking, a differentiable approximation of ranking from [31]. We use the default parameters given from the official PyTorch [53] implementation. Finally, plugging in the soft rank approximation $\hat{R_{\max}}(X_i)$ to the saliency metric, summing over the set P, and negating for minimization, the saliency loss function, which we minimize with gradient descent, is:

$$L_{\Delta\text{-saliency}} = -\sum_{i \in \{(a,b) | a \in \text{Image},, b \in \text{Reference points}\}} \frac{\mathbb{I}\Big(R(Y_{\text{LAB},i}) - \hat{R_{\max}}(X_i) + \Delta > 0\Big) \cdot \hat{R_{\max}}(X_i)^\gamma}{\sum_i \hat{R_{\max}}(X_i)^\gamma}$$

In all experiments, we set $\Delta = 0$ and $\gamma = 2$ in the loss function, based on the hypothesis that this would enhance the detection of rare objects, such as plaques or neurons. However, these values could be further refined. As previously noted, this parameter assigns greater weight to larger distance ranks, which may help in identifying rare objects. A lower value of γ, such as 0 or 0.5, could potentially improve overall performance while reducing effectiveness in rare sub-groups. Further investigations into this trade-off would be valuable in future work. As a strategy for selecting reference points for optimization, we consider the following options:

- **Lightweight core sets method** [10]. This method is a fast sampling method that samples points for both diversity and coverage of the main clusters.
- **K-means++** [11], which selects points in a way that maximizes their spread: the first point is chosen randomly, and subsequent points are sampled with probability proportional to their squared distance from the nearest existing centroid.
- **Random sampling**.

Supplementary Information, Figure 18 shows the effect of different sampling strategies. For a large number of points, the difference is smaller; however, run time will increase (the complexity is proportional to the number of reference points). Cosine distance correlation performs better with K-means++; however, this is somewhat expected because the distance function in K-means++ is Euclidean.

By default, we use the lightweight core sets method [10] for sampling reference points because of its speed. For optimization, we use the Adam optimizer [54] with a learning rate of 1. The visualization is initialized with a random normal distribution in the range [-5, 5].

Spearman Rank Correlation Optimization. The Spearman visualization method is similar to SALO, however, the objective is to maximize the Spearman rank correlation between the maximum rank of the cosine and L_∞ distances in the high- and low-dimensional data. This provides a simpler and more natural alternative to the saliency objective, which we use as a baseline to verify its positive impact.

Lightweight visualizations. TOP3 selects the three highest intensity values per pixel and then maps them to the LAB color space. We implement this method efficiently using the Numba Python package. Our Percentile Ratio (PR3D) visualization is a generalization of TOP3, measuring how intensities are distributed. We define the PR function, which operates on pixel coordinates i and j for two fixed percentiles p_1 and p_2:

$$\lambda(X_{ij,p_1,p_2}) = \frac{\text{Percentile}(X_{ij}, p_1)}{\text{Percentile}(X_{ij}, p_2)}$$

The L, A, and B channels in the LAB color space are then computed as follows:

$$\begin{aligned} L_{ij} &= \lambda(X_i j, p1, p2) = \lambda(X_{ij}, 99.99\%, 99.9\%) \\ A_{ij} &= \lambda(X_i j, p2, p3)\lambda(X_{ij}, 99.9\%, 99\%) \\ B_{ij} &= \lambda(X_i j, p4, p5)\lambda(X_{ij}, 98\%, 85\%) \end{aligned}$$

The percentiles p_1, p_2 and p_3 were selected by a grid search on the first image of the mouse brain dataset (containing 5,255 features), evaluating 1,000 predefined combinations within the range [85%, 100%]. The values of p_4 and p_5 were manually adjusted to achieve the desired pink shade. Future work may focus on making these values differentiable for direct optimization or developing a more efficient search method.

Interactive m/z mapping methods

Region selection. MSI-VISUAL facilitates the automatic selection of regions by interacting with the visualization. One method for this is based on the approach by

Felzenszwalb et al. [29], a classical, efficient, and fast graph-based computer vision algorithm that performs spatial segmentation of images into sub-regions, accounting for both spatial arrangement and visual appearance. An alternative method supported by MSI-VISUAL involves segmentation of color channels without using spatial information. In this case, each of the three color channels (Red, Green, and Blue) in the visualization is segmented into N sub-regions (with $N = 5$ by default, though this can be adjusted). Segmentation is achieved by digitizing each channel into N equally spaced bins in the range $[0, 1]$:

$$\text{Segment}_{ij} = \text{Digitized(Red)}_{ij} \cdot N^2 + \text{Digitized(Green)}_{ij} \cdot N + \text{Digitized(Blue)}_{ij}$$

Here, i and j denote the pixel coordinates, Digitized(image) represents the quantization of an image or region into N bins, and Segment_{ij} refers to the sub-region to which pixel (i, j) belongs.

Region vs. region comparisons. For a pair of selected regions, the Area Under the Curve (AUC) is computed between the two groups. We then perform statistical analysis on the m/z values, selecting those with a p-value<0.05 to identify m/z values that significantly differ between the compared regions.

Region vs. all comparisons. In this mode, the user selects a single region for comparison with the entire image. A complementary mask is created for the selected region, and to speed up the comparison, every second pixel of the complementary mask is sub-sampled.

Point-to-Point comparisons. In this mode, users select pairs of points by clicking on them within the visualization. For each m/z value in the spectra of a point, we compute its rank within the image. The rank difference between the two selected points is then calculated, and the m/z values are sorted by this rank difference. A positive rank difference indicates that a particular m/z value is more prominent in the first point, while a negative rank difference implies that the m/z value is more prominent in the second point.

Presenting the Results: The SpectrumQR (SpecQR) visualization method The goal of the SpecQR visualization is to provide an interpretable visual signature of statistically identified m/z values, enabling rapid assessment of molecular differences between ROIs. The input to SpecQR is a list of discriminative m/z values between two regions, along with their associated statistical scores.

In the first part of the SpecQR visualization, we generate a summary ion image, using the Cividis color scheme [30], by averaging the five m/z values with the highest statistical scores. This image offers a high-level overview of spatial signal intensity corresponding to the most discriminative features.

In the second part, we produce a 2D spectrum visualization covering the total acquired m/z range. Each "pixel" in this 2D grid corresponds to a single m/z value and is color-coded by its statistical score. This allows users to visually identify global patterns in molecular signatures between regions and quickly assess their molecular similarity and distinguishing features. An in-depth example is shown in Supplementary Information, Figure 15.

Additionally, we include a bi-color overlay visualization, in which one region is encoded in red and the other in green, offering an intuitive spatial comparison between their molecular profiles.

Presenting the Results: Interactive Exploration of m/z Values To support interactive exploration, the list of significant m/z values is presented to the user, ranked by their statistical score. Users can click on any entry to instantly generate a Virtual Pathology Stain, described in the following section, for visual verification.

This interactive workflow enables rapid and intuitive exploration of anatomical differences. Fine-grained anatomical features are first revealed using the visualization methods, followed by user-guided region selection. Regions are then compared using SpecQR, allowing users to visually inspect and refine region selection and verify or dismiss m/z values based on their spatial patterns.

Presenting the results: The Virtual Pathology Stain (VPS). To simulate a commonly used immunohistochemical (IHC) stain, the grayscale ion intensity images were mapped to a brown color scale. Total ion current (TIC) intensities of fully resolved m/zs were normalized for each m/z to 0-1 for all pixels, and a linear interpolation was performed for each pixel between white (RGB: 255, 255, 255) and dark brown (RGB: 139, 69, 19). This mapping ensures that low-intensity pixels remain light, while high-intensity regions are rendered in progressively deeper shades of brown, visually resembling 3,3'-diaminobenzidine (DAB) staining used in IHC pathology.

Quantitative evaluation of the MSI visualizations

Evaluation metrics. As the evaluation metric, we use the Distance Pearson correlation, which quantifies how well pairwise distances are preserved between high-dimensional and low-dimensional spaces. Specifically, we computed the Euclidean distances between all pairs of points (pixels) in the original high-dimensional MSI data and separately between the corresponding points in the three-dimensional RGB space used for visualization. We then compute the Pearson correlation between these two sets of distances. A higher correlation indicates better preservation of the global structure of the high-dimensional data in the reduced RGB representation. This approach has previously been applied to MSI visualization evaluation [19] and is a well-established metric to evaluate dimensionality reduction [33, 55]. Following prior work in MSI visualization [19] and to assess performance under different distance metrics corresponding to different biological scenarios of m/z differences between regions, we computed correlations using both Cosine and L_∞ distances (Supplementary Information, Figure 19). The distance L_∞ is defined as the maximum absolute difference in intensity between all m/z values between two pixels.

In addition, we report benchmarking with similar results for the Spearman rank correlation metric (Supplementary Information, Figure 23), and our Saliency metric (Supplementary Information, Figure 22) that have not been used before for evaluating MSI, which may be meaningful for future comparisons.

Benchmarking of the MSI visualizations. We evaluated the new visualization methods on two datasets:

i) A mouse model brain dataset (Supplementary Information, Table 1) consisting of four brain hemisphere scans at 20µm resolution. This dataset represents controlled, high-quality MSI data, where special care has been taken in sample preparation and the measurement protocol.
ii) A diverse collection of six datasets from the METASPACE repository [9] (Supplementary Information, Table 2), covering various tissue types, low and high resolutions, different numbers of features, and different m/z ranges. Some scans were created with peak selection, reducing the number of features. Some image files are huge, making them computationally challenging to process.

Only our proposed methods (SALO, SPEAR, TOP3, and PR3D), along with PaCMAP, PCA, and NMF, were able to run on the full-size images using a high-performance machine with 320GB of RAM. To facilitate comparisons with all methods on the second dataset, we subsampled every second pixel from the large kidney (dataset 4) and lung (dataset 6) MS images.

Data availability

Our mouse brain dataset files are available on the ProteomeXchange PRIDE repository with the dataset number PXD056609.

Code availability

We are releasing the code for the visualizations and GUI as an open-source package on Github: MSI-VISUAL.

Acknowledgments

The authors would like to thank Dr. Jorunn Stamnæs for performing the MSI measurements of the mouse brains and for technical discussions, and Thomas Brüning for cutting and preparing the mouse brain hemispheres and the H&E and immunohistochemistry stains. The mass spectrometry-based analyzes of mouse brains were performed at the Proteomics Core Facility at the University of Oslo/Oslo University Hospital, which is supported by the Core Facilities Program of the South-Eastern Norway Regional Health Authority (HSØ) and NAPI (www.napi.uio.no, NFR, Norway; 295910).

The authors would like to thank Dr.-Ing. Marcin Grzegorzek, Professor at the Institute of Medical Informatics, University of Lübeck/Germany, for supporting our work.

The authors would also like to thank Dr. Jörg Hanrieder, Professor at the University of Gothenburg, for his comments on our manuscript.

The authors would like to thank Manuel Liebeke (MPI Bremen, Germany), Michaela Schwaiger-Haber (Washington University in St. Louis, USA), Tingting Lu (South China Agricultural University, China), Brittney Gorman and Dušan Veličković (Pacific Northwest National Laboratory, USA) for sharing their datasets as open-access on METASPACE.

The authors would like to thank especially Lars Gruber, Thomas Enzlein, and Carsten Hopf (Hochschule Mannheim, Germany) for sharing their datasets directly with us and on METASPACE.

The datasets were used for benchmarking and in Figures 3, 7, 8, 10, and 12, as well as for figure 17 in the Supplementary Information.

Ethical approval

The animal study protocol and breeding were approved by the KPM Forsøksdyrutvalget and Mattilsynet (IV2-2022, FOTS 20540).

Author contributions

J.G. analyzed the MSI data and wrote and revised the manuscript. J.P. analyzed the MSI data, wrote and revised the manuscript, acquired funding, and provided infrastructure.

Competing interests

The authors declare no competing interests.

Funding

J.P. received funding from Norges forskningsråd (NFR, Norway; 327571 (PETABC), 295910 (NAPI, www.napi.uio.no)), and the EIC Pathfinder Open Challenges program (EU commission; 101185769).

References

[1] Shimma S. Mass Spectrometry Imaging [Journal Article]. Mass Spectrom (Tokyo). 2022;11(1):A0102. https://doi.org/10.5702/massspectrometry.A0102.

[2] Alexandrov T. Spatial Metabolomics and Imaging Mass Spectrometry in the Age of Artificial Intelligence [Journal Article]. Annu Rev Biomed Data Sci. 2020;3:61–87. https://doi.org/10.1146/annurev-biodatasci-011420-031537.

[3] Nuñes JB, Ijsselsteijn ME, Abdelaal T, Ursem R, van der Ploeg M, Giera M, et al. Integration of mass cytometry and mass spectrometry imaging for spatially resolved single-cell metabolic profiling [Journal Article]. Nat Methods. 2024;21(10):1796–1800. https://doi.org/10.1038/s41592-024-02392-6.

[4] Zhang H, Lu KH, Ebbini M, Huang P, Lu H, Li L. Mass spectrometry imaging for spatially resolved multi-omics molecular mapping [Journal Article]. Npj Imaging. 2024;2(1):20. https://doi.org/10.1038/s44303-024-00025-3.

[5] Farrow MA, Tideman LEM, Neumann EK, Migas LG, Patterson NH, Colley ME, et al. A lipid atlas of the human kidney [Journal Article]. Sci Adv. 2025;11(24):eadu3730. https://doi.org/10.1126/sciadv.adu3730.

[6] Schramm T, Hester Z, Klinkert I, Both P, Heeren RMA, Brunelle A, et al. imzML – A Common Data Format for the Flexible Exchange and Processing of Mass Spectrometry Imaging Data. Journal of Proteomics. 2012;75(16):5106–5110. https://doi.org/10.1016/j.jprot.2012.07.026.

[7] Bemis KA, Foll MC, Guo D, Lakkimsetty SS, Vitek O. Cardinal v.3: a versatile open-source software for mass spectrometry imaging analysis [Journal Article]. Nat Methods. 2023;20(12):1883–1886. https://doi.org/10.1038/s41592-023-02070-z.

[8] Zhang Y, Wang X, Li M, Guo T, Zhao Z, Zhang X, et al. An easy-to-use graphical user interface for mass spectrometry imaging analysis [Journal Article]. International Journal of Mass Spectrometry. 2023;492. https://doi.org/10.1016/j.ijms.2023.117105.

[9] Alexandrov T, Ovchinnikova K, Palmer A, Kovalev V, Tarasov A, Stuart L, et al. METASPACE: A community-populated knowledge base of spatial metabolomes in health and disease. bioRxiv. 2019;https://doi.org/10.1101/539478.

[10] Bachem O, Lucic M, Krause A. Scalable k-Means Clustering via Lightweight Coresets [Journal Article]. arXiv. 2017;https://doi.org/10.48550/arxiv.1702.08248.

[11] k-means++: the advantages of careful seeding. Society for Industrial and Applied Mathematics; 2007. Available from: https://theory.stanford.edu/~sergei/papers/

kMeansPP-soda.pdf.

[12] Hu H, Yin R, Brown HM, Laskin J. Spatial Segmentation of Mass Spectrometry Imaging Data by Combining Multivariate Clustering and Univariate Thresholding [Journal Article]. Anal Chem. 2021;93(7):3477–3485. https://doi.org/10.1021/acs.analchem.0c04798.

[13] Zhang W, Claesen M, Moerman T, Groseclose MR, Waelkens E, De Moor B, et al. Spatially aware clustering of ion images in mass spectrometry imaging data using deep learning [Journal Article]. Anal Bioanal Chem. 2021;413(10):2803–2819. https://doi.org/10.1007/s00216-021-03179-w.

[14] Buchberger AR, DeLaney K, Johnson J, Li L. Mass Spectrometry Imaging: A Review of Emerging Advancements and Future Insights [Journal Article]. Anal Chem. 2018;90(1):240–265. https://doi.org/10.1021/acs.analchem.7b04733.

[15] Verbeeck N, Caprioli RM, Van de Plas R. Unsupervised machine learning for exploratory data analysis in imaging mass spectrometry [Journal Article]. Mass Spectrom Rev. 2020;39(3):245–291. https://doi.org/10.1002/mas.21602.

[16] McInnes L, Healy J, Melville J. UMAP: Uniform Manifold Approximation and Projection for Dimension Reduction. arXiv preprint arXiv:180203426. 2018;https://doi.org/10.48550/arXiv.1802.03426.

[17] Smets T, Verbeeck N, Claesen M, Asperger A, Griffioen G, Tousseyn T, et al. Evaluation of Distance Metrics and Spatial Autocorrelation in Uniform Manifold Approximation and Projection Applied to Mass Spectrometry Imaging Data. Analytical Chemistry. 2019;91(9):5706–5714. https://doi.org/10.1021/acs.analchem.8b05827.

[18] Kohonen T. Self-Organized Formation of Topologically Correct Feature Maps. Biological Cybernetics. 1982;43(1):59–69. https://doi.org/10.1007/BF00337288.

[19] Gardner W, Maliki R, Cutts SM, Muir BW, Ballabio D, Winkler DA, et al. Self-Organizing Map and Relational Perspective Mapping for the Accurate Visualization of High-Dimensional Hyperspectral Data [Journal Article]. Anal Chem. 2020;92(15):10450–10459. https://doi.org/10.1021/acs.analchem.0c00986.

[20] Huang H, Wang Y, Rudin C, Browne EP. Towards a comprehensive evaluation of dimension reduction methods for transcriptomic data visualization [Journal Article]. Commun Biol. 2022;5(1):719. https://doi.org/10.1038/s42003-022-03628-x.

[21] Pearson K. On Lines and Planes of Closest Fit to Systems of Points in Space. Philosophical Magazine. 1901;2(11):559–572. https://doi.org/10.1080/14786440109462720.

[22] Hyvarinen A. Fast and robust fixed-point algorithms for independent component analysis [Journal Article]. IEEE Trans Neural Netw. 1999;10(3):626–34. https://doi.org/10.1109/72.761722.

[23] Tenenbaum JB, de Silva V, Langford JC. A global geometric framework for nonlinear dimensionality reduction [Journal Article]. Science. 2000;290(5500):2319–23. https://doi.org/10.1126/science.290.5500.2319.

[24] Lee DD, Seung HS. Learning the parts of objects by non-negative matrix factorization. Nature. 1999;401:788–791. https://doi.org/10.1038/44565.

[25] van der Maaten L, Hinton G. Visualizing Data using t-SNE. Journal of Machine Learning Research. 2008;9:2579–2605.

[26] Amid E, Warmuth MK. TriMap: Large-scale Dimensionality Reduction Using Triplets. ArXiv. 2019;abs/1910.00204. https://doi.org/10.48550/arXiv.1910.00204.

[27] Wang Y, Huang H, Rudin C, Shaposhnik Y. Understanding how dimension reduction tools work: an empirical approach to deciphering t-SNE, UMAP, TriMap, and PaCMAP for data visualization. J Mach Learn Res. 2021;22(1). https://doi.org/10.5555/3546258.3546459.

[28] Moon KR, van Dijk D, Wang Z, Chen W, Hirn MJ, Coifman RR, et al. PHATE: a dimensionality reduction method for visualizing trajectory structures in high-dimensional biological data [Journal Article]. BioRxiv. 2017;120378. https://doi.org/10.1038/s41587-019-0336-3.

[29] Felzenszwalb PF, Huttenlocher DP. Efficient Graph-Based Image Segmentation. International Journal of Computer Vision. 2004;59(2):167–181. https://doi.org/10.1023/B:VISI.0000022288.19776.77.

[30] Nuñez JR, Anderton CR, Renslow RS. Optimizing colormaps with consideration for color vision deficiency to enable accurate interpretation of scientific data [Journal Article]. PLoS One. 2018;13(7):e0199239. https://doi.org/10.1371/journal.pone.0199239.

[31] Blondel M, Teboul O, Berthet Q, Djolonga J. Fast Differentiable Sorting and Ranking [Journal Article]. arXiv. 2020;https://doi.org/10.48550/arXiv.2002.08871.

[32] Spearman C. The Proof and Measurement of Association Between Two Things. The American Journal of Psychology. 1904;15(1):72–101. https://doi.org/10.2307/1412159.

[33] Lee JA, Verleysen M. Quality assessment of dimensionality reduction: Rank-based criteria. Neurocomputing. 2009;72(7-9):1431–1443. https://doi.org/10.1016/j.

neucom.2008.06.011.

[34] Bascunana P, Brackhan M, Pahnke J. Machine Learning-Supported Analyses Improve Quantitative Histological Assessments of Amyloid-beta Deposits and Activated Microglia [Journal Article]. J Alzheimers Dis. 2021;79(2):597–605. https://doi.org/10.3233/JAD-201120.

[35] Santos-García I, Bascuñana P, Brackhan M, Villa M, Eiriz I, Brüning T, et al. The ABC transporter A7 modulates neuroinflammation via NLRP3 inflammasome in Alzheimer's disease mice [Journal Article]. Alzheimer's Research & Therapy. 2025;17(1):30. https://doi.org/10.1186/s13195-025-01673-2.

[36] Ge J, Koutarapu S, Jha D, Dulewicz M, Zetterberg H, Blennow K, et al. Tetramodal Chemical Imaging Delineates the Lipid-Amyloid Peptide Interplay at Single Plaques in Transgenic Alzheimer's Disease Models [Journal Article]. Anal Chem. 2023;95(10):4692–4702. https://doi.org/10.1021/acs.analchem.2c05302.

[37] Koutarapu S, Ge J, Dulewicz M, Srikrishna M, Szadziewska A, Wood J, et al. Chemical imaging delineates Abeta plaque polymorphism across the Alzheimer's disease spectrum [Journal Article]. Nat Commun. 2025;16(1):3889. https://doi.org/10.1038/s41467-025-59085-7.

[38] Gildenblat J, Stamnaes J, Pahnke J. MSI-ATLAS: Mass spectrometry imaging and explainable machine learning uncover the brain's lipid landscapes. bioRxiv. 2025;https://doi.org/10.1101/2025.09.12.675752. https://www.biorxiv.org/content/early/2025/09/17/2025.09.12.675752.full.pdf.

[39] Wood JI, Dulewicz M, Szadziewska A, Weiner S, Ge J, Stringer K, et al. Isotope-encoded spatial biology identifies plaque-age-dependent maturation and synaptic loss in an Alzheimer's disease mouse model [Journal Article]. Nat Commun. 2025;16(1):8170. https://doi.org/10.1038/s41467-025-63328-y.

[40] Brackhan M, Calza G, Lundgren K, Bascunana P, Bruning T, Soliymani R, et al. Isotope-labeled amyloid-beta does not transmit to the brain in a prion-like manner after peripheral administration [Journal Article]. EMBO Rep. 2022;23(7):e54405. https://doi.org/10.15252/embr.202154405.

[41] Xie YR, Castro DC, Rubakhin SS, Trinklein TJ, Sweedler JV, Lam F. Multiscale biochemical mapping of the brain through deep-learning-enhanced high-throughput mass spectrometry. Nat Methods. 2024;21(3):521–530. https://doi.org/10.1038/s41592-024-02171-3.

[42] Schwaiger-Haber M, Stancliffe E, Anbukumar DS, Sells B, Yi J, Cho K, et al. Using mass spectrometry imaging to map fluxes quantitatively in the tumor ecosystem [Journal Article]. Nat Commun. 2023;14(1):2876. https://doi.org/10.1038/s41467-023-38403-x.

[43] Enzlein T, Lashley T, Sammour DA, Hopf C, Chavez-Gutierrez L. Integrative Single-Plaque Analysis Reveals Signature Abeta and Lipid Profiles in the Alzheimer's Brain [Journal Article]. Anal Chem. 2024;96(24):9799–9807. https://doi.org/10.1021/acs.analchem.3c05557.

[44] Gruber L, Schmidt S, Enzlein T, Vo HG, Bausbacher T, Cairns JL, et al. Deep MALDI-MS spatial omics guided by quantum cascade laser mid-infrared imaging microscopy [Journal Article]. Nat Commun. 2025;16(1):4759. https://doi.org/10.1038/s41467-025-59839-3.

[45] Hanrieder J, Malmberg P, Lindberg OR, Fletcher JS, Ewing AG. Time-of-flight secondary ion mass spectrometry based molecular histology of human spinal cord tissue and motor neurons [Journal Article]. Anal Chem. 2013;85(18):8741–8. https://doi.org/10.1021/ac401830m.

[46] Mendis LH, Grey AC, Faull RL, Curtis MA. Hippocampal lipid differences in Alzheimer's disease: a human brain study using matrix-assisted laser desorption/ionization-imaging mass spectrometry [Journal Article]. Brain Behav. 2016;6(10):e00517. https://doi.org/10.1002/brb3.517.

[47] Veloso A, Fernandez R, Astigarraga E, Barreda-Gomez G, Manuel I, Giralt MT, et al. Distribution of lipids in human brain [Journal Article]. Anal Bioanal Chem. 2011;401(1):89–101. https://doi.org/10.1007/s00216-011-4882-x.

[48] Prasad M, Postma G, Franceschi P, Buydens LMC, Jansen JJ. Evaluation and comparison of unsupervised methods for the extraction of spatial patterns from mass spectrometry imaging data (MSI) [Journal Article]. Sci Rep. 2022;12(1):15687. https://doi.org/10.1038/s41598-022-19365-4.

[49] Radde R, Bolmont T, Kaeser SA, Coomaraswamy J, Lindau D, Stoltze L, et al. Abeta42-driven cerebral amyloidosis in transgenic mice reveals early and robust pathology [Journal Article]. EMBO Rep. 2006;7(9):940–6. https://doi.org/10.1038/sj.embor.7400784.

[50] Andersen MK, Hoiem TS, Claes BSR, Balluff B, Martin-Lorenzo M, Richardsen E, et al. Spatial differentiation of metabolism in prostate cancer tissue by MALDI-TOF MSI [Journal Article]. Cancer Metab. 2021;9(1):9. https://doi.org/10.1186/s40170-021-00242-z.

[51] Kibbe RR, Muddiman DC. Quantitative mass spectrometry imaging (qMSI): A tutorial. Journal of Mass Spectrometry. 2024;59(4):e5009. https://doi.org/10.1002/jms.5009.

[52] Winsor CP. Robust Estimation and Winsorization. Bulletin of the Harvard University Public Health. 1941;23:179–184.

[53] Paszke A, Gross S, Massa F, Lerer A, Bradbury J, Chanan G, et al. PyTorch: an imperative style, high-performance deep learning library. Curran Associates Inc.; 2019.

[54] Kingma DP, Ba J. Adam: A Method for Stochastic Optimization. arXiv preprint arXiv:14126980. 2014;https://doi.org/10.48550/arXiv.1412.6980.

[55] Sainburg T, McInnes L, Gentner TQ. Parametric UMAP embeddings for representation and semi-supervised learning. arXivorg. 2021;https://doi.org/10.48550/arXiv.2009.12981. [cs.LG].

[56] Sunkin SM, Ng L, Lau C, Dolbeare T, Gilbert TL, Thompson CL, et al. Allen Brain Atlas: an integrated spatio-temporal portal for exploring the central nervous system [Journal Article]. Nucleic Acids Res. 2013;41(Database issue):D996–D1008. https://doi.org/10.1093/nar/gks1042.

Supplementary information

Benchmarking visualizations and K-means segmentation

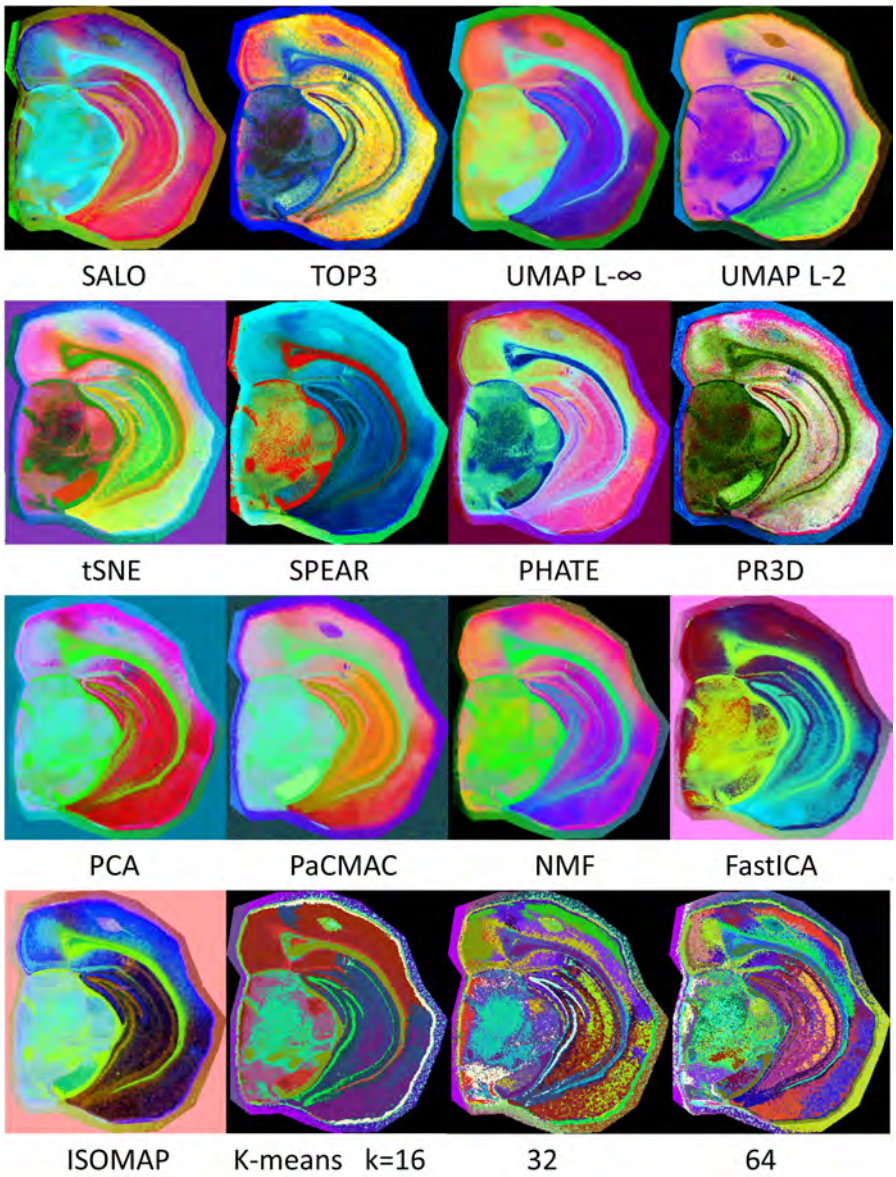

Fig. 13 Comparison of benchmarking visualisations and K-means segmentations. Note the smooth color gradients of the visualizations in the RGB color space versus the strict cluster colors used to highlight the K-means segmentation. K-means is useful for observing anatomical regions; however, inter-cluster anatomical details are invisible because all pixels are assigned the same color.

K-means segmentation

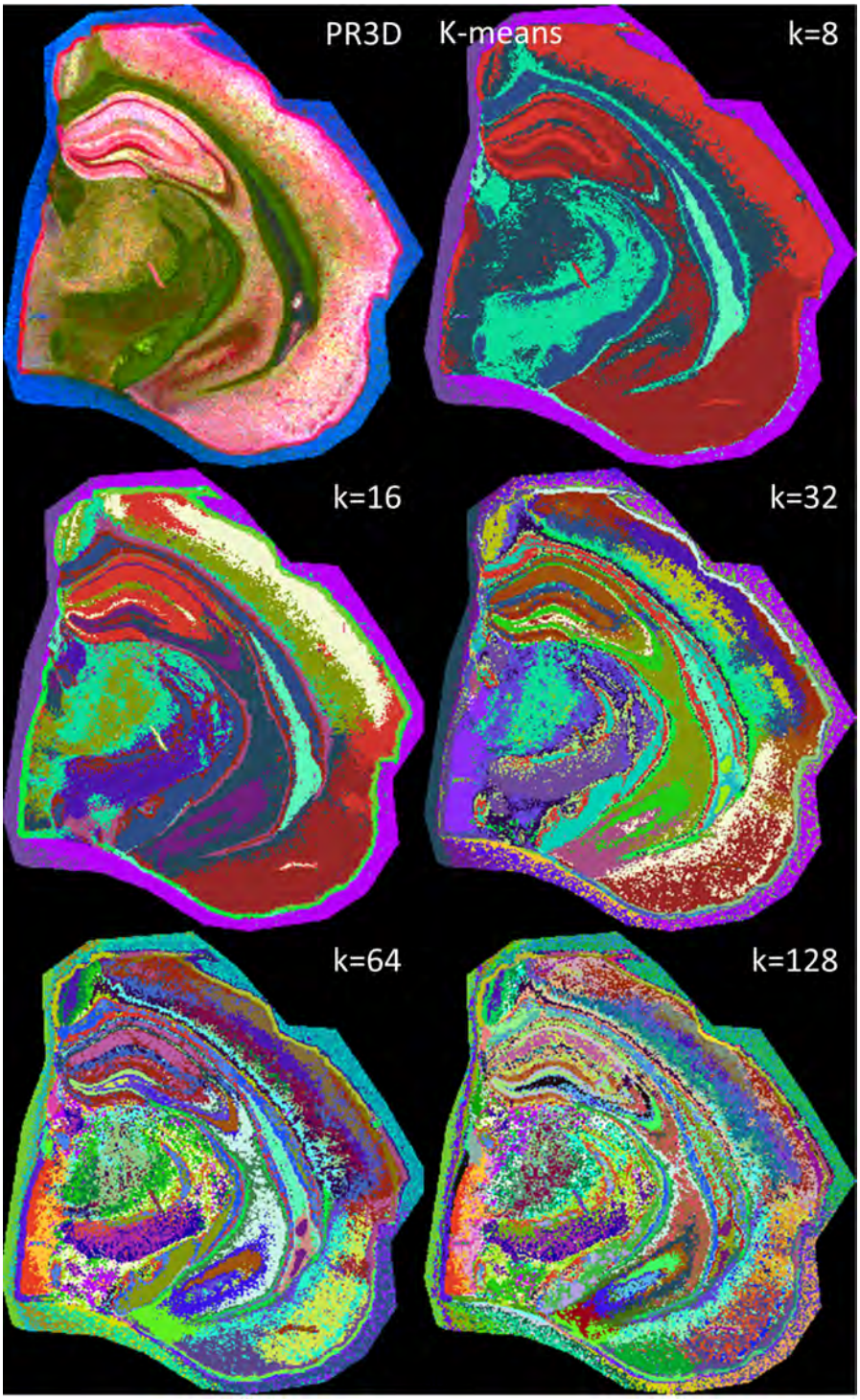

Fig. 14 K-means loses inter-cluster anatomical detail and misses small structures compared to continuous value RGB visualization methods. Shown are the proposed PR3D DR visualization alongside five K-means segmentations ($k = 8 - 128$) of the same dataset. While K-means is effective for identifying and distinguishing broad anatomical regions, it often fails to capture finer structures, such as plaques, which are not assigned a distinct cluster. This limitation arises from K-means assigning the same color to all pixels within a cluster, resulting in a loss of intra-cluster anatomical detail compared to the continuous representation provided by PR3D. Increasing the number of clusters (higher k) can reveal more fine-grained details, but this often comes at the cost of interpretability and usability, making precise region annotation more challenging. Although K-means remains a practical and widely used tool in MSI analysis, we advocate for the broader adoption of continuous-value, dimensionality reduction-based visualization methods to complement clustering approaches and enhance anatomical and molecular interpretability.

The SpectrumQR graph (SpecQR)

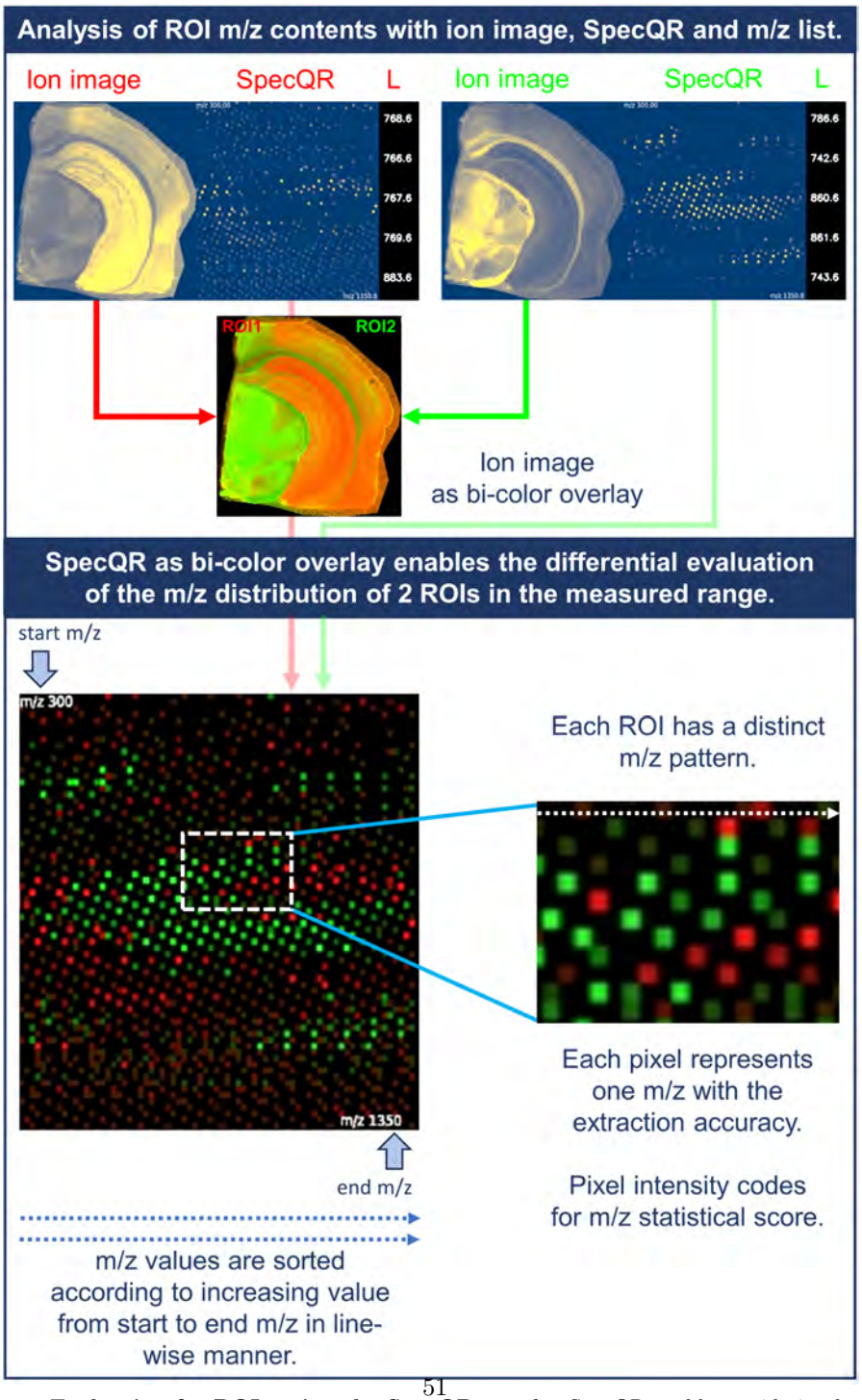

Fig. 15 Evaluation for ROIs using the SpecQR graph. SpecQR enables rapid visual assessment of m/z differences between selected regions of interest. The input to SpecQR is a list of m/z values that statistically differentiate between two regions, along with their associated scores. First, for each region, we generate a summary ion image by summing the grayscale images corresponding to the top five m/z values (L) with the highest statistical scores. This provides a quick spatial overview of region-specific molecular signatures. Next, we display the full list of m/z values in a 2D grid spanning the acquired m/z range, where each pixel represents a single m/z value. The intensity of each pixel is modulated by the statistical score, allowing users to quickly identify which parts of the spectrum contribute most to regional differences.
Finally, we include a bi-color overlay visualization that combines both regions into a single image —m/z values enriched in one region are shown in red, while those enriched in the other are shown in green— offering an intuitive summary of molecular contrasts.

Binning effect on advanced and lightweight visualizations

Here, we present two panels to show the effects of data binning before dimensionality reduction:

- a hemisphere of our mouse brain dataset with 20µm pixel resolution (Table 1)
- a dataset from METASPACE (Table 2, dataset 5) of a mouse spinal cord with 5µm pixel resolution (Figure 10)

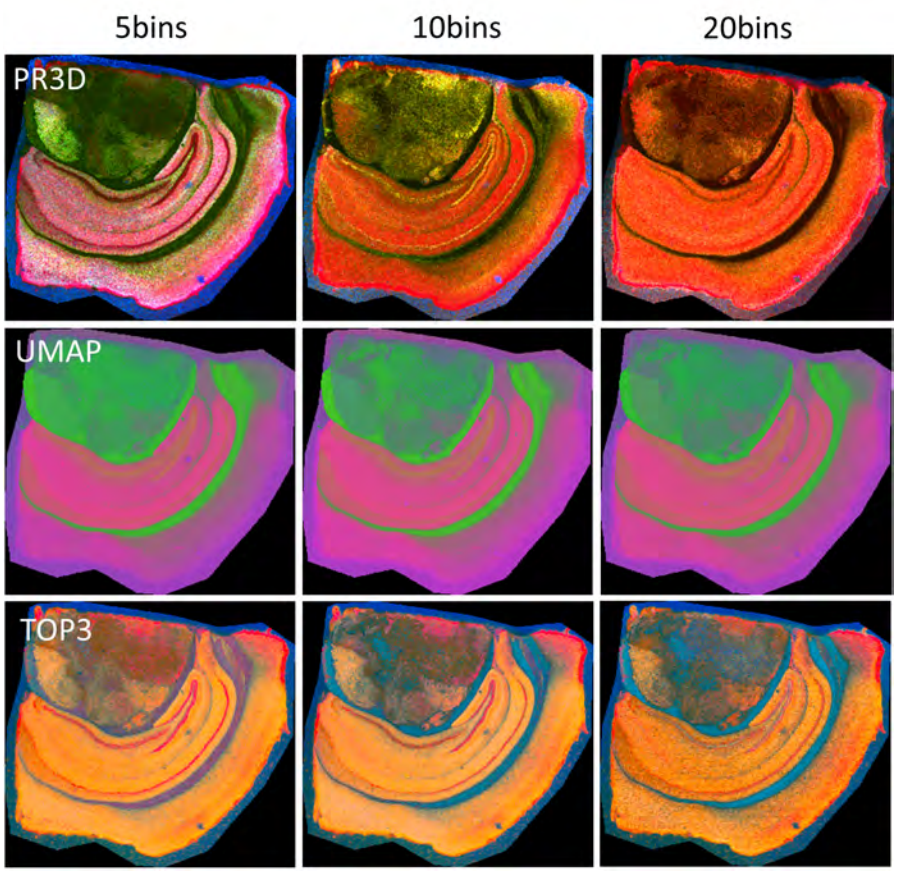

Fig. 16 Overview of the effects of different binning for the visualizations of hippocampus details. Binning with 5, 10, and 20 bins per Dalton (respectively $0.2 = 200mDa$, $0.1 = 100mDa$, and $0.05 = 50mDa$ m/z value precision) shows slight effects for the lightweight visualization methods PR3D and TOP3, with 5 bins highlighting optimal visualization characteristics in the hippocampus. UMAP, as a more complex DR method, is only minor affected by the different binning ranges.

To compare binning effects on the spinal cord dataset visualizations, we used an extensive panel of the following methods:

1. K-means: k=8, max-iter:200, color-scheme:gist-rainbow
2. K-means: k=16, max-iter:200, color-scheme:gist-rainbow
3. K-means: k=32, max-iter:200, color-scheme:gist-rainbow
4. K-means: k=64, max-iter:200, color-scheme:gist-rainbow
5. Non-Parametric UMAP: min-dist: 0.5, n-neighbors: 100, metric: euclidean
6. Non-Parametric UMAP: min-dist: 0.5, n-neighbors: 500, metric: euclidean
7. NMF3D: max-iter=200
8. NMF3D: max-iter=1000
9. NMF clustering: k=8, max-iter=2000, spatial-norm
10. NMF clustering: k=16, max-iter=2000, spatial-norm
11. NMF clustering: k=32, max-iter=2000, spatial-norm
12. PR3D: static percentiles
13. SALO: num-epochs: 200, regularization-strength: 0.001, sampling: coreset, number-of-points:1000
14. SALO: num-epochs: 200, regularization-strength: 0.01, sampling: coreset, number-of-points:1000
15. SPEAR: num-epochs: 200, regularization-strength: 0.001, sampling: coreset, number-of-points:1000
16. TOP3: low=99.9

Fig. 17 Overview of the effects of binning on advanced and lightweight visualizations. We used of a 5µm-resolution dataset of mouse spinal cord and performed binning with 5 (12GB npy-file size), 10 (24GB), 20 (48GB), and 40 (96GB) bins per Dalton (respectively $0.2 = 200mDa$, $0.1 = 100mDa$, $0.05 = 50mDa$, and $0.025 = 25mDa$ precision). High spectral resolution (= high number of bins) has extensive computational and memory requirements. The effects of binning strongly depend on the chosen visualization / dimensionality-reduction method:
The lightweight visualization TOP3 is not influenced by binning at all. PR3D shows the best result using 5 bins. Our new advanced visualization methods, SALO and SPEAR, are resistant to binning. NMF3D shows only slight differences between the different binning. However, UMAP shows strong noise problems in the 40 bins extraction. Clustering methods (K-means, NMF) are heavily influenced by binning, depending on the number of clusters and binning, with 5 bins showing the best output. Note the visualization quality decrease for K-means or NMF towards higher bins. The visualizations left blank in the 40-bins column could not be performed due to computational restrictions. We used 320GB RAM and 64GB GPU memory.
Summarizing, to generate truthful visualizations for large datasets, binning with 5 bins delivers the needed quality.

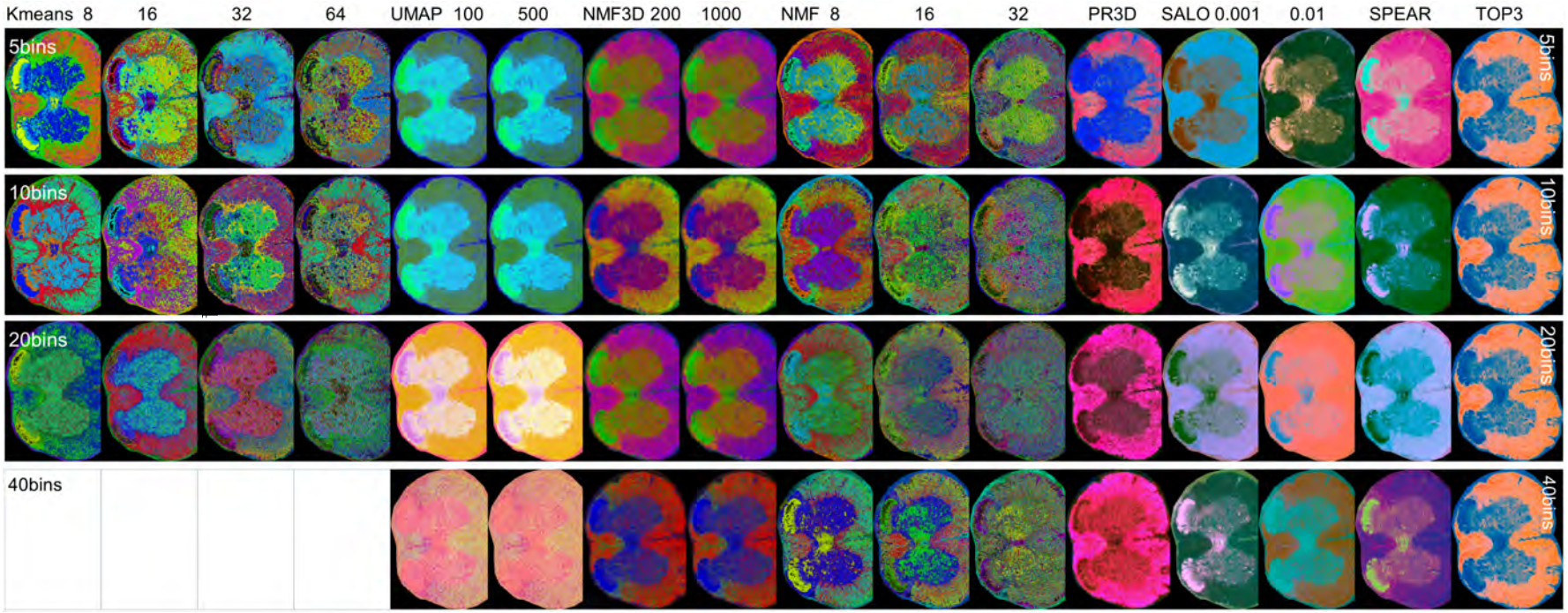
Kmeans 8
16
32
64
UMAP 100
500
NMF3D 200
1000
NMF 8
16
32
PR3D
SALO 0.001
0.01
SPEAR
TOP3
5bins
10bins
20bins
40bins

Reference point selection and visualization metrics

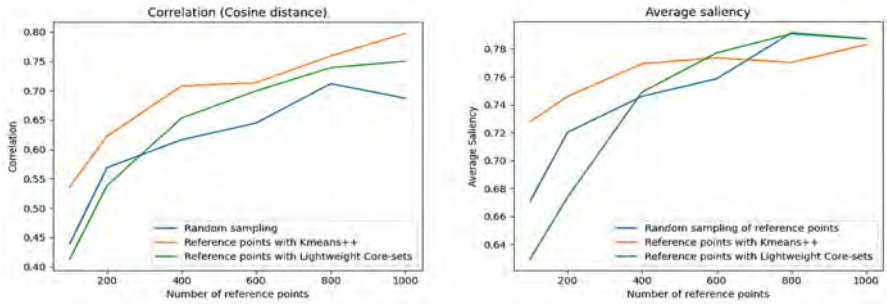

Fig. 18 Comparison of reference point selection methods on visualization metrics.

The benchmarking datasets

Image size	Features	Tissue type	Resol.	Npy file size
286×262	5255	Mouse brain hemisphere (hA7ko)	20µm	1.5GB
331×248	5255	Mouse brain hemisphere (APPPS1 × hA7ko)	20µm	1.7GB
314×294	5255	Mouse brain hemisphere (APPPS1)	20µm	1.9GB
314×285	5255	Mouse brain hemisphere (C57BL/6J wild-type)	20µm	1.8GB

Table 1 Dataset characteristics for the mouse brain benchmarking dataset (PXD056609). The mouse models were recently described in [35].

Link	Image size	Features	Uploader	Tissue type	Resol.	Npy file size
Dataset 1	62×160	4505	Manuel Liebeke (MPI Bremen)	Bacterial vesicles	100µm	175MB
Dataset 2	135×199	1755	Schwaiger-Haber et al. [42]	Brain with tumor (mouse)	50µm	184MB
Dataset 3	104×108	4285	Tingting Lu	Ovary (mouse)	20µm	188MB
Dataset 4	550×824	5255	Brittney Gorman (PNNL)	Kidney (human)	5µm	9.3GB
Dataset 5	521×417	10505	Lars Gruber (HS Mannheim)	Spinal cord (mouse)	5µm	8.9GB
Dataset 6	772×596	16505	Dušan Veličković (PNNL)	Lung (human)	20µm	30GB

Table 2 Dataset characteristics for the diverse benchmarking dataset with slides from METASPACE [9].

Benchmarking results

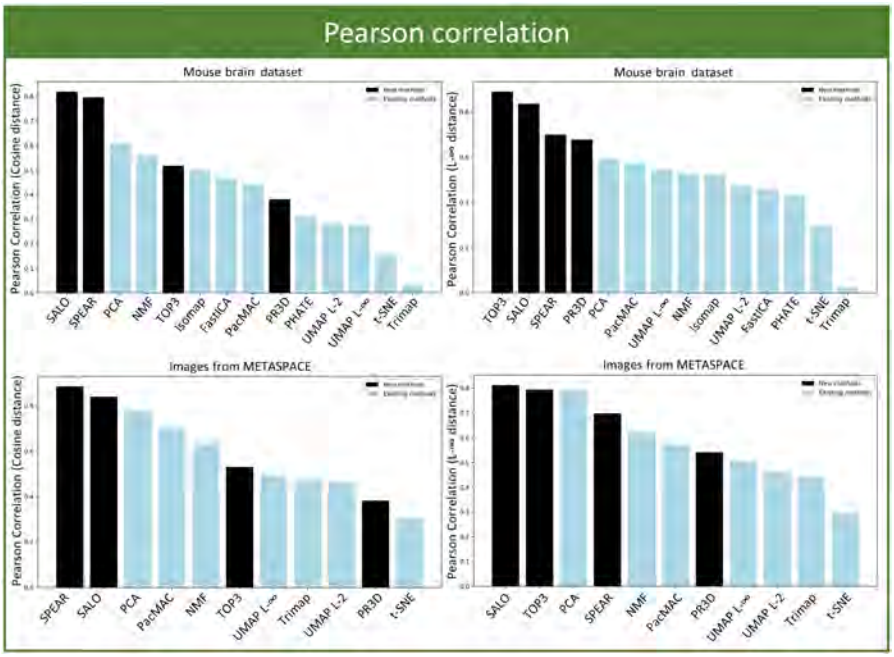

Fig. 19 Benchmarking of MSI visualization methods. The results are sorted from higher (better) to lower. The proposed methods are colored in black (SALO, SPEAR, PR3D, and TOP3). SALO outperforms all existing methods (light blue) were as SPEAR is behind PCA using the METASPACE dataset and L_∞ distance.

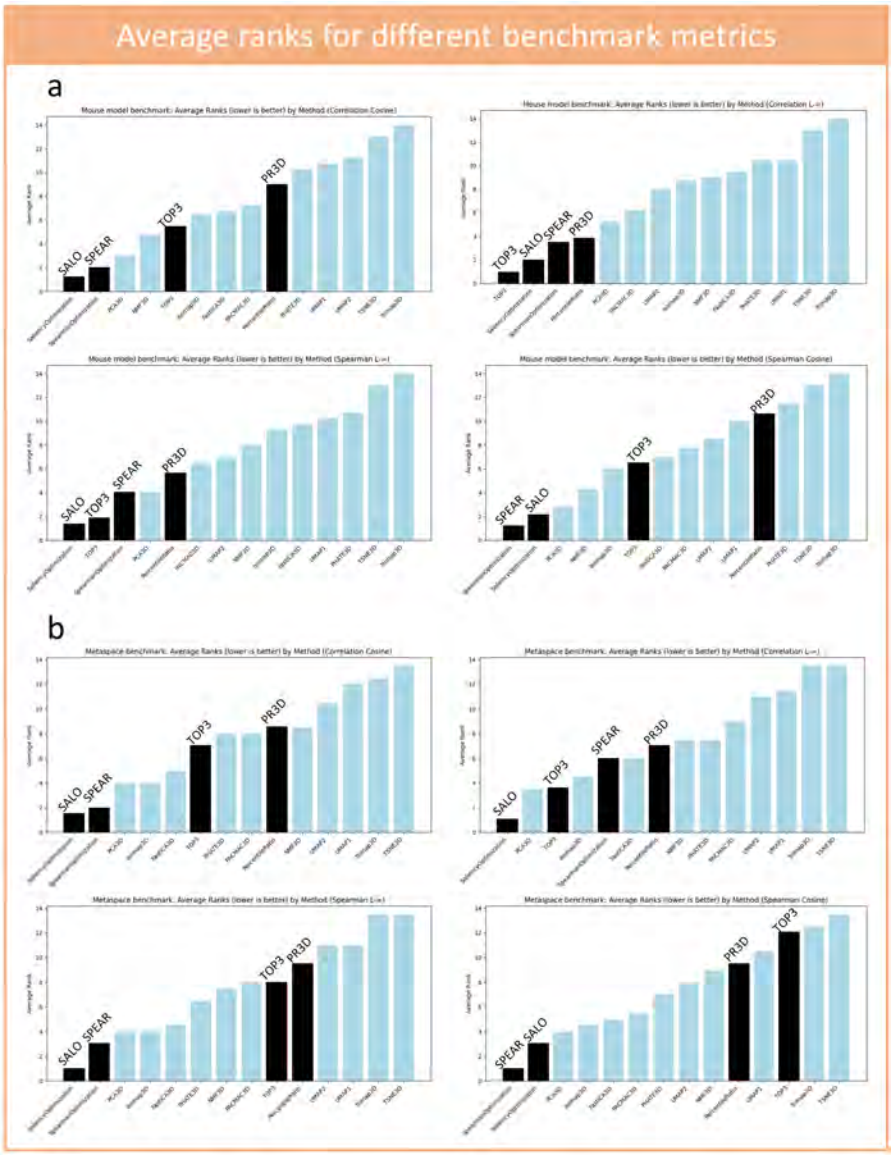

Fig. 20 Benchmarking of MSI visualization methods - Ranking. **a** Ranking of the visualizations using the mouse brain dataset. **b** Ranking of the visualizations using the mouse brain dataset. A lower average rank is better. The proposed methods are in black. SALO outperforms all formerly existing methods in competition with SPEAR (Spearman cosine metrics, both datasets) or TOP3 (L_∞ distance metrics, mouse dataset) on all metrics and datasets.

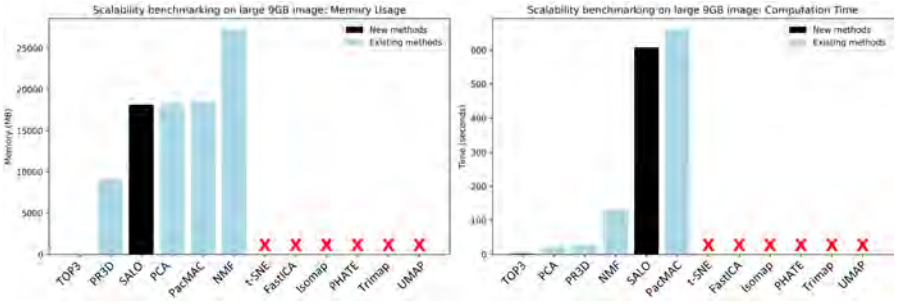

Fig. 21 Benchmarking MSI visualization memory and speed on large images. The proposed, new methods are shown as black bars. TOP3 is 600× faster to run and consumes only 2**M**B RAM compared to 25**G**B for NMF and 17**G**B for SALO and PaCMAP. Methods that could not run due to resource needs (>320GB RAM) are marked with ×.

Here, we share more benchmarking results with custom metrics that have not been used before for MSI. We share these for additional future comparison, as it may be valuable to collect more metrics for evaluation, but do not place them in the main text to avoid confusion about our method's performance with the established metrics used before for MSI. Supplementary Information, Figure 22 shows the benchmark results for our custom Saliency metric. Supplementary Information, Figure 23 shows the benchmark result for the Spearman correlation metric. Our SALO is the best method in all datasets. TOP3 and PR don't perform well on the METASPACE dataset under the Cosine distance.

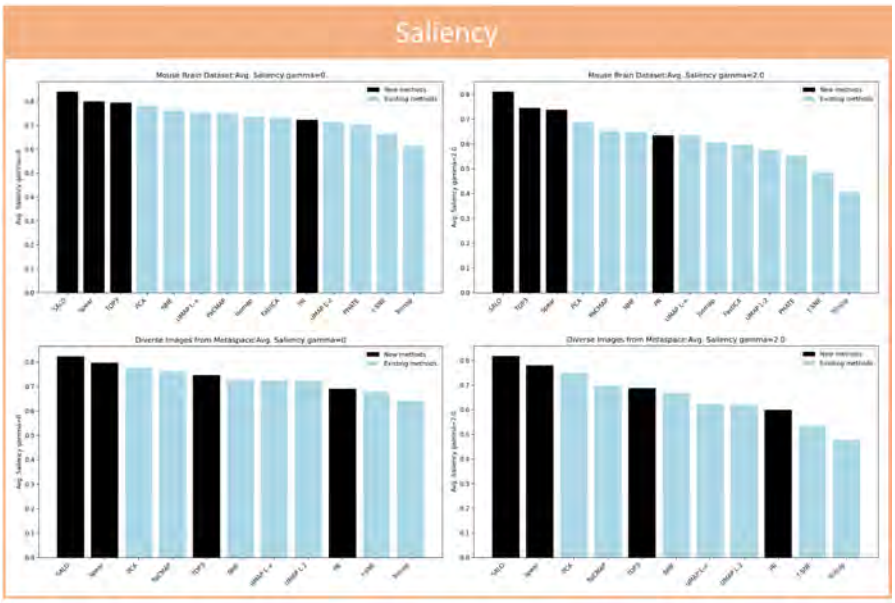

Fig. 22 Benchmarking results for MSI visualizations using the proposed Saliency metric. The proposed methods are colored in black (SALO, SPEAR, PR3D, and TOP3).

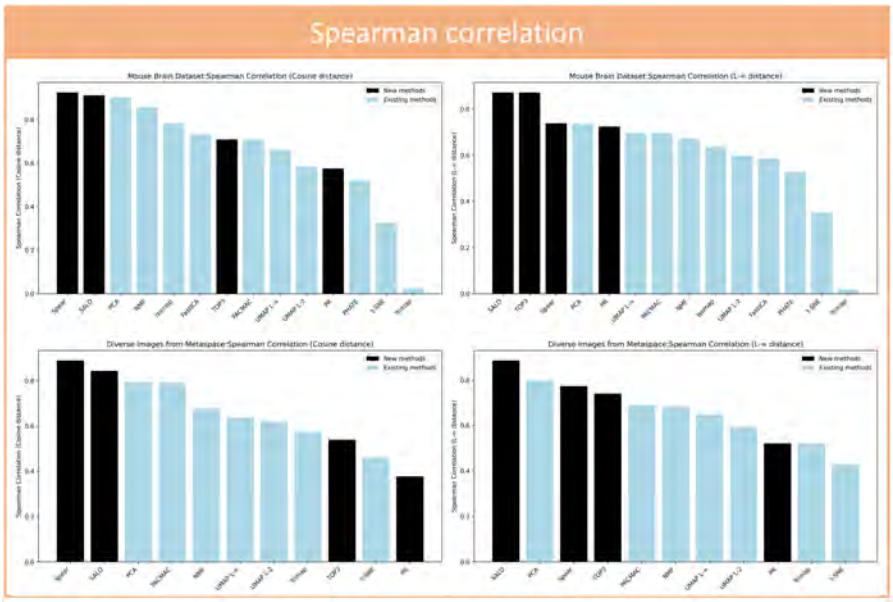

Fig. 23 Benchmarking results for MSI visualizations using the Spearman rank correlation metric. The proposed methods are colored in black (SALO, SPEAR, PR3D, and TOP3).

Detecting pathological changes in parenchymal organs - kidney

For the diagnostics of diseases in surgical pathology, several stainings are usually produced each with a preference for different tissue behavior or pathological changes. We generated different visualizations using MSI-VISUAL, highlighting various levels of detail and specificity, similar to immunohistochemical stains, however, using a lipid MSI (sample information in Table 2).

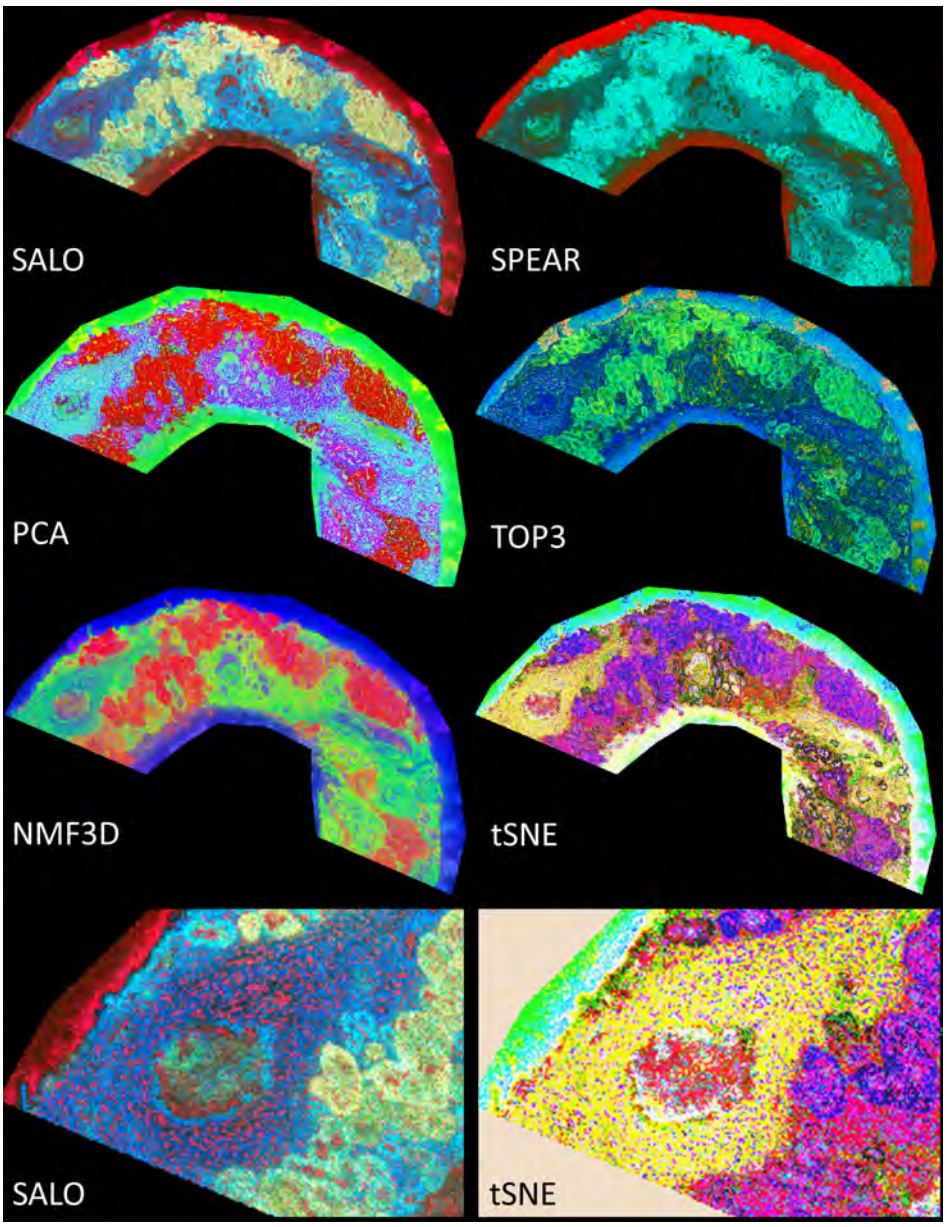

Fig. 24 Overview of SALO, SPEAR, PCA, TOP3, NMF3D, and t-SNE visualizations revealing different levels of anatomical details. The zoomed-in figures highlight a glomerulum with extensive inflammation and loss of different kidney tubuli (blue in SALO, yellow in t-SNE), the red pixels in SALO and the red/violet pixels in t-SNE highlight putative inflammatory cells (lymphocytes). The different parts of the kidney tubulus system (proximal, distal) are best seen in the SALO and t-SNE visualizations.

Detecting functional details of hippocampal connections

Figures 25 and 26 show an overview of UMAP, SALO, SPEAR, PR3D, and TOP3 and conventional HE and immunohistochemical stains of one hemisphere of our mouse brain dataset (Table 1). The images show a coronal cut mouse brain hemisphere at bregma position –3.08 mm of a C57BL/6J mouse (commonly used B6 genetic background strain) and a schematic representation of the same location in the Allen mouse brain atlas [56]. UMAP reveals some gross details in the brain stem, e.g. the thalamus (TH) regional differences, the substantia nigra (SN), but also details in the hippocampus formation (HPF, green region in the Allen atlas), such as dentate gyrus (DG neurons) and to a lesser extent Cornu Ammonis field 3 neurons (CA3). Regarding the hippocampus formation (HPF), SALO, Spear, and PR3D reveal more details than UMAP and TOP3, with PR3D showing contrasted neuronal bands (CA1 and CA3, DG, all in dark pinkish) versus connections between them (layered pinkish or greenish). SPEAR especially highlights the molecular layer of the DG (DG-mo). PR3D highlights the layering and different extent of myelination of the cortex (CTX, degree of myelination as extent of the green signal). TOP3 shows a clear representation of the neuronal bands of the hippocampus formation (red, CA1, CA3, and DG) versus an orange background.

Figure 5 shows a zoomed-in cross-section of the hippocampal structures, revealing different levels of detail. UMAP often shows a homogeneous area and misses very distinct anatomical features (arrow 1 - basal layer of the dentate gyrus, arrow 2 - neurons in CA1) that are visible in the new visualizations. Arrow 3 points to single cells detected in the dentate gyrus isthmus using PR3D.

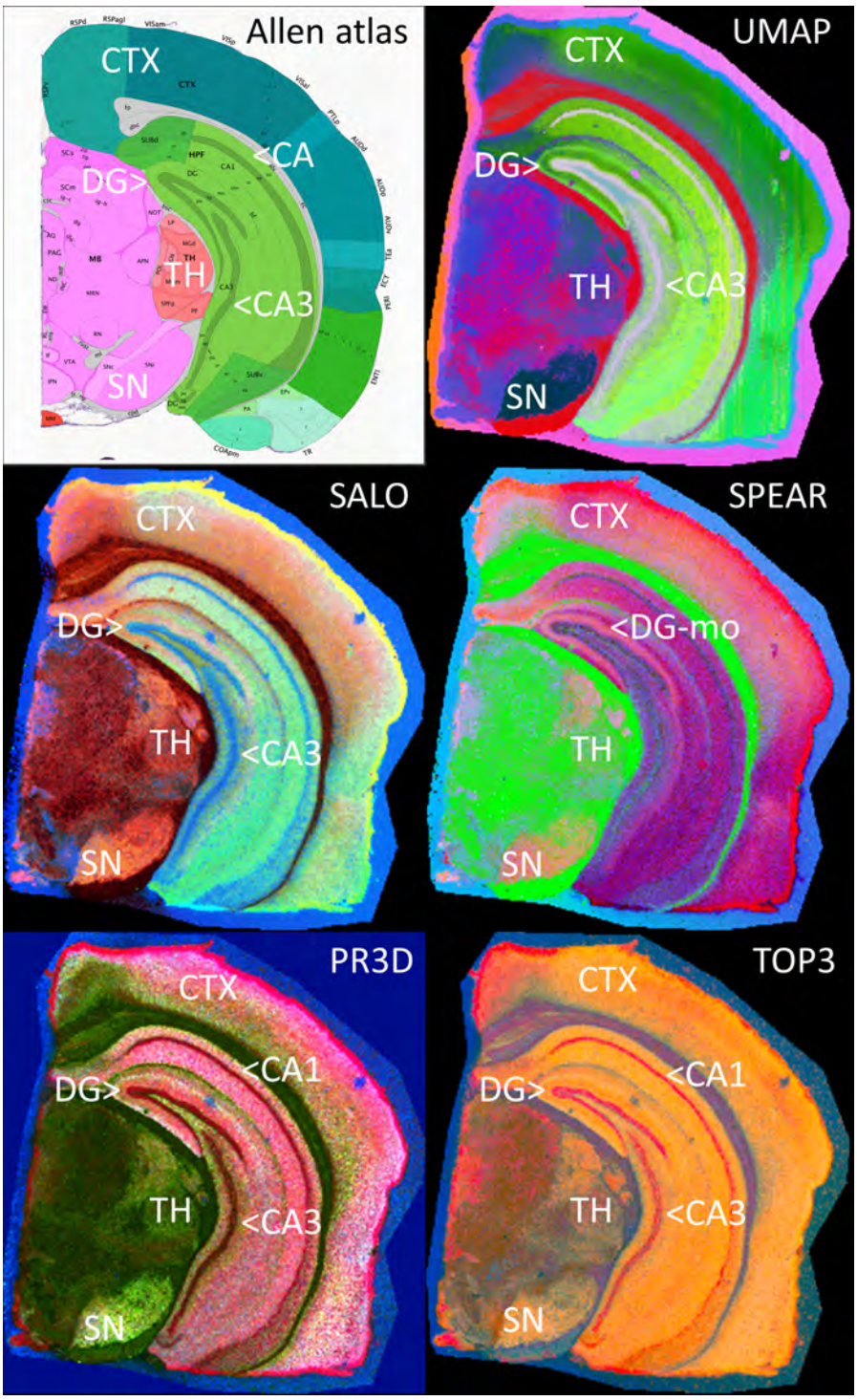

Fig. 25 Overview of UMAP, SALO, SPEAR, PR3D, and TOP3 visualizations revealing different levels of anatomical details, e.g. in thalamus (TH), Substantia nigra (SN), hippocampus, and brain stem related to global data structure preservation. Legend: CTX, isocortex; CA1, Cornu Ammonis field 1; CA3, Cornu Ammonis field 3; DG, dentate gyrus; TH, thalamus.

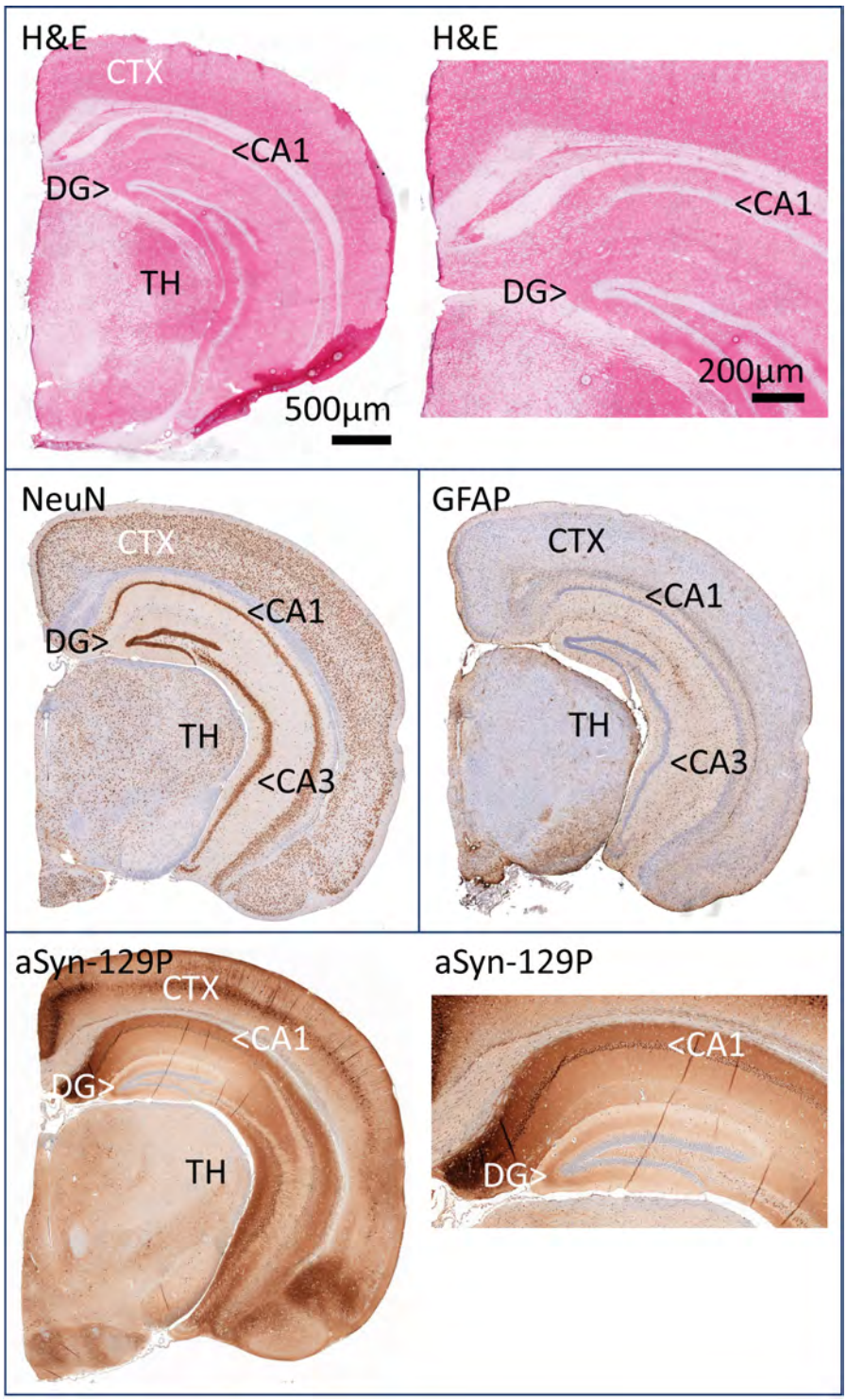

Fig. 26 Overview of mouse brain hemispheres stained using a H&E conventional pathology stain (from the frozen tissue blocks) and three immunohistological stains (IHC, from FFPE blocks): NeuN for neurons, GFAP for astrocytes, and αSyn-129P for neurons and processes showing positivity for phosphorylated α-synuclein. The H&E stain magnification of the hippocampus formation is less detail-rich than the MSI visualizations of the lipidomics dataset (Supplementary Information, Figure 25). The IHC stains show specific details that the MSI lipidomics visualizations can reveal in a single dataset, e.g., the hippocampus layering between DG and CA1. Legend: CTX, isocortex; CA1, Cornu Ammonis field 1; CA3, Cornu Ammonis field 3; DG, dentate gyrus; TH, thalamus.

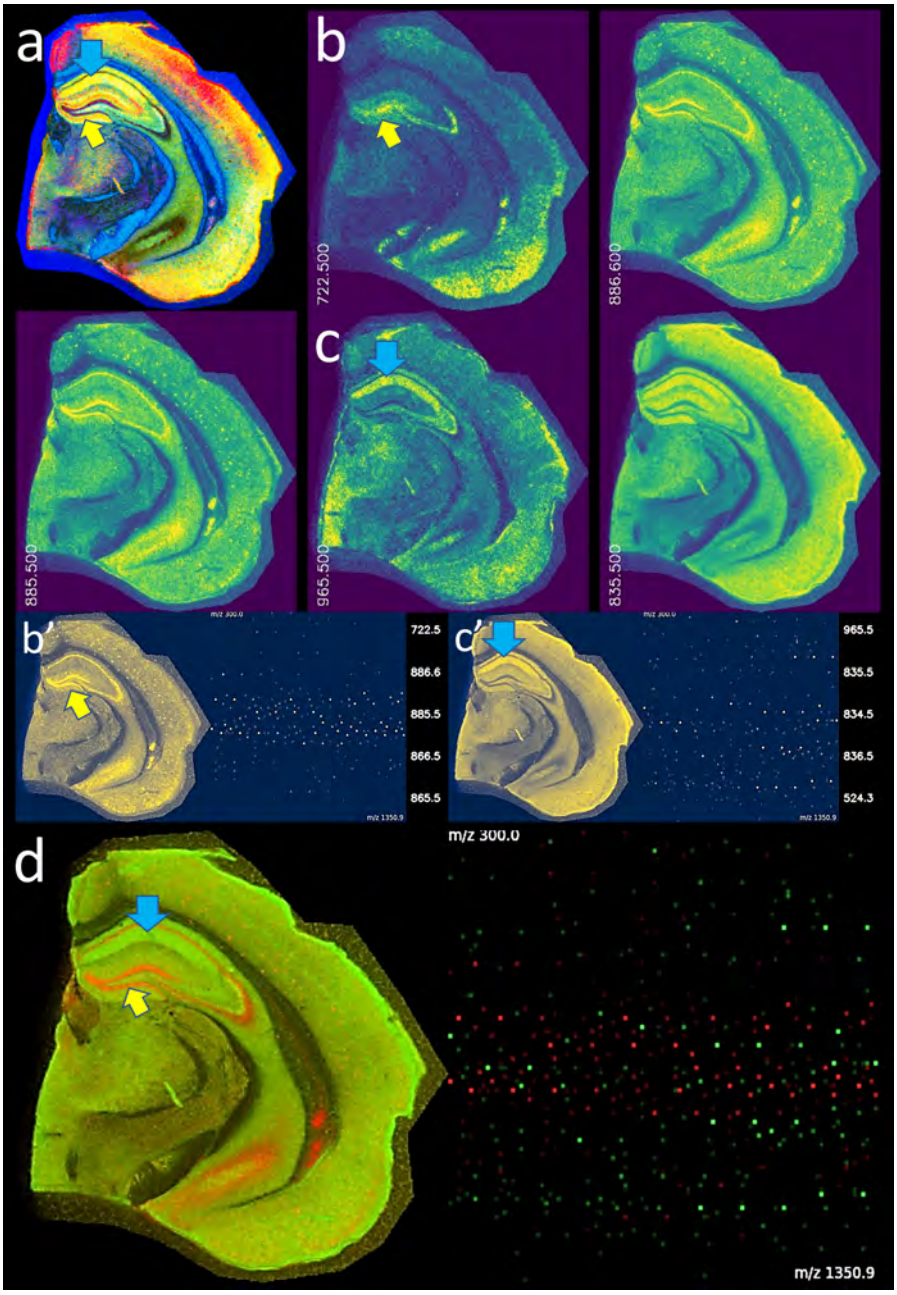

Fig. 27 Differential visualization and functional segmentation of lipids in hippocampal connections. **a** TOP3 visualization of a brain hemisphere. The yellow arrow points to the dentate gyrus neurons (DG granule cell layer, dark band) and the blue arrow towards axonal processes of the Cornu Ammonis neurons (CA1 stratum radiale, yellow band). These were selected for further analysis. **b** shows the three best m/z ion images (722.5, 885.5, 886.6) corresponding to the selected location for detection (yellow arrow). **b'** shows the aggregated ion image of the 5 best m/z values (list on the right) and the SpecQR graph. **c** shows the two best m/z ion images (965.5, 835.5) and the selected CA1 stratum radiale (blue arrow). **c'** shows the aggregated ion image of the 5 best m/z values (list on the right) and the SpecQR graph. **d** shows a red-green overlay image of both aggregated ion images from the selected regions and the SpecQR in the corresponding colors. The SpecQR diagram shows the m/z distribution from m/z 300-1350 with very distinct, not overlapping m/z values for both structures. Note the detection of Aβ plaques in b' and d (red channel) labeled with m/z 722.5 and 885.5/886.6 (M+1).

Histopathological 'ground truth' – the H&E stain

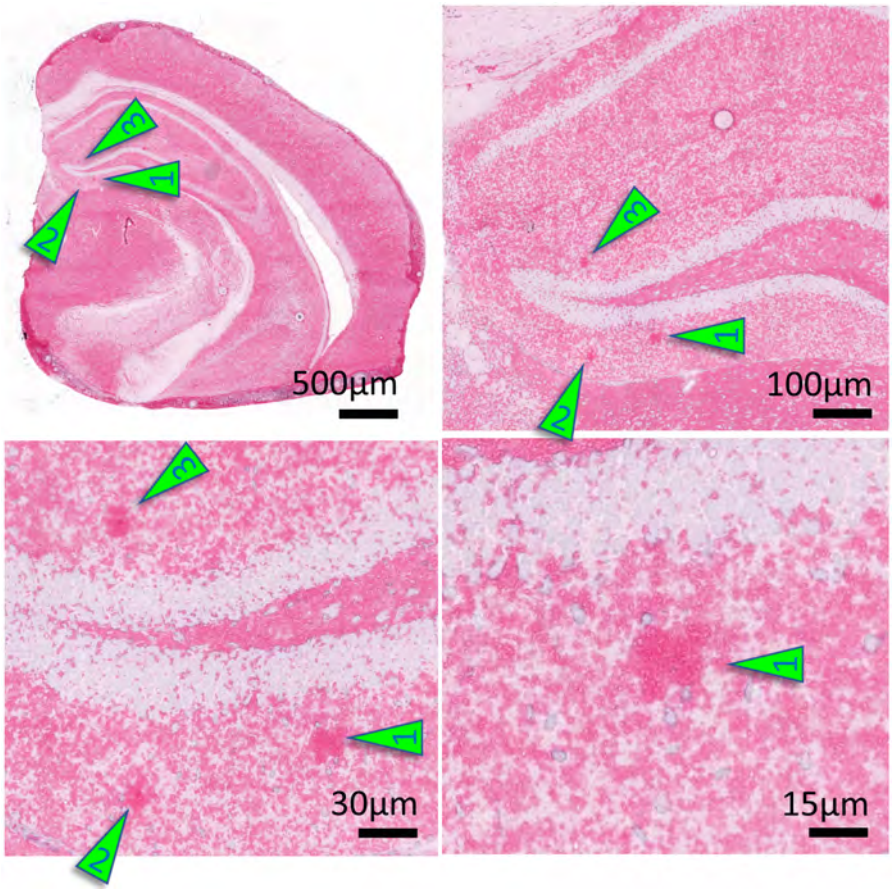

Fig. 28 Overview of a brain hemisphere of the APPtg-positive mouse from Figure 6 using a H&E pathology stain (from the same frozen tissue block) with numerous cortical and hippocampal plaques. The arrows point towards condensed eosinophilic protein aggregates of Aβ in the hippocampal formation at different magnifications. Arrow 1 corresponds to the plaque that is highlighted in the Results section, Figure 6 with a red arrow. The plaque core size can be estimated to be approximately 20µm in diameter.